

Different degrees of nitrogen and carbon depletion in the warm molecular layers of protoplanetary disks

KENJI FURUYA,¹ SEOKHO LEE,² AND HIDEKO NOMURA^{1,3}

¹*National Astronomical Observatory of Japan, Osawa 2-21-1, Mitaka, Tokyo 181-8588, Japan*

²*Korea Astronomy and Space Science Institute, 776 Daedeok-daero, Yuseong-gu, Daejeon 34055, Republic of Korea*

³*Department of Astronomical Science, The Graduate University for Advanced Studies (SOKENDAI), Osawa, Mitaka, Tokyo 181-8588, Japan*

(Received; Revised; Accepted)

Submitted to ApJ

ABSTRACT

Observations have revealed that the elemental abundances of carbon and oxygen in the warm molecular layers of some protoplanetary disks are depleted compared to those in the interstellar medium by a factor of ~ 10 –100. Meanwhile, little is known about nitrogen. To investigate the time evolution of nitrogen, carbon, and oxygen elemental abundances in disks, we develop a one-dimensional model that incorporates dust settling, turbulent diffusion of dust and ices, as well as gas-ice chemistry including the chemistry driven by stellar UV/X-rays and the galactic cosmic rays. We find that gaseous CO in the warm molecular layer is converted to CO₂ ice and locked up near the midplane via the combination of turbulent mixing (i.e., the vertical cold finger effect) and ice chemistry driven by stellar UV photons. On the other hand, gaseous N₂, the main nitrogen reservoir in the warm molecular layer, is less processed by ice chemistry, and exists as it is. Then the nitrogen depletion occurs solely by the vertical cold finger effect of N₂. As the binding energy of N₂ is lower than that of CO and CO₂, the degree of nitrogen depletion is smaller than that of carbon and oxygen depletion, leading to higher elemental abundance of nitrogen than that of carbon and oxygen. This evolution occurs within 1 Myr and proceeds further, when the α parameter for the diffusion coefficient is $\sim 10^{-3}$. Consequently, the N₂H⁺/CO column density ratio increases with time. How the vertical transport affects the midplane ice composition is briefly discussed.

Keywords: astrochemistry — protoplanetary disks — ISM: molecules

1. INTRODUCTION

Formation of planets occurs in protoplanetary disks. The elemental compositions of gas and solids in disks directly set the elemental compositions of forming planets in the disks. Understanding the elemental compositions of gas and solids in disks is thus the first step in understanding how planets acquire their compositions (e.g., Öberg & Bergin 2021).

Recent observations have found that elemental abundances of volatile carbon and oxygen in some disks are different from those in the interstellar medium (ISM).

In the three disks (TW Hya, DM Tau, and GM Aur), where gas mass is measured with the HD line observations (Bergin et al. 2013; McClure et al. 2016), the CO abundance in the warm molecular layer ($T \gtrsim 20$ K) is lower than the canonical value of 10^{-4} by factors of 10–100 (e.g., Favre et al. 2013; Zhang et al. 2019, 2021). As CO is the major carrier of volatile carbon, a reasonable hypothesis is that volatile elemental carbon is depleted in the gas phase by similar factors. Survey observations of disks in nearby star-forming regions have found that CO emission is much weaker than expected, even when the freeze-out of CO onto dust grains and photodissociation by stellar UV photons are considered in disk models (Ansdell et al. 2016; Long et al. 2017; Miotello et al. 2017). The faint CO emission may indicate that the CO abundance in the warm molecu-

lar layer in disks is typically lower than the canonical value. Alternatively, it may indicate that gas mass of H_2 is lower than expected in the disks. The timescale of carbon (and oxygen) depletion has been suggested to be fast (~ 1 Myr), based on the observations of CO isotopologues towards disks in different evolutionary stages/ages (Bergner et al. 2020b; Zhang et al. 2020). In addition, some disks show brighter C_2H emission than expected, indicating the C/O ratio higher than unity at least in the C_2H emitting regions (Bergin et al. 2016; Miotello et al. 2019; Bosman et al. 2021b). The high C/O ratio indicates that the degree of oxygen depletion is more significant than that of carbon.

There are some proposed mechanisms to explain the depletion of volatile carbon and oxygen in the warm molecular layer: conversion of CO into less volatile species through chemistry driven by cosmic-rays/X-rays (e.g., Bergin et al. 2014; Furuya & Aikawa 2014), so-called vertical cold finger effect (e.g., Meijerink et al. 2009; Kama et al. 2016; Xu et al. 2017), and a combination of both of these (Krijt et al. 2020). The vertical cold finger effect is the phenomena as follows; Turbulence brings the gaseous molecules from the warm molecular layer to the disk midplane, where the dust temperature is low and molecules are frozen out onto large dust grains. As large dust grains are not fully coupled with the turbulent gas motion, they are settled close to the midplane, trapping ices on them. As a result, the abundances of gaseous molecules in the disk atmosphere can decrease with time.

Compared to carbon and oxygen, our understanding of the nitrogen elemental abundance in disks is rather limited. The main carrier of nitrogen in the warm molecular layer is expected to be N_2 or atomic N in the gas phase (e.g., Li et al. 2013), which are not directly observable. Some observational studies have concluded that the degree of nitrogen depletion is significantly smaller than that of carbon and oxygen. Cleeves et al. (2018) concluded that carbon and oxygen are depleted in the observable gas of the IM Lup disk compared to the ISM elemental abundances by a factor of ~ 20 or even larger, whereas nitrogen is not significantly depleted (up to a factor of four compared to the ISM elemental abundance), based on the observations of CO, C_2H , and HCN and the physical-chemical modeling of the disk. The estimated age of IM Lup is 0.5–1 Myr (Mawet et al. 2012), again indicating the timescale of carbon and oxygen depletion is fast. Anderson et al. (2019) found that the $\text{N}_2\text{H}^+/\text{CO}$ flux ratio in 5–11 Myr old disks in Upper Scorpius is higher than that in $\lesssim 2$ Myr old disks, including the IM Lup disk. The high $\text{N}_2\text{H}^+/\text{CO}$ flux ratio in the older disks may indicate that N_2 , which is the

parent molecule of N_2H^+ , is less impacted by the physical and chemical processes in disks, and remains in the gas phase for longer timescale than CO. It also may indicate that the degree of carbon depletion continues to be enhanced over time after ~ 2 Myr.

In addition to the elemental composition in disks, nitrogen abundance is relevant to the measurements of the disk gas mass; Trapman et al. (2022) showed that the combination of C^{18}O line and N_2H^+ line can be a good prove of disk gas mass, assuming that N_2 is not depleted in the disk gas. One of the biggest uncertainties to measure the disk gas mass is the CO abundance in the warm molecular layer, as it is not necessarily the canonical value of 10^{-4} as mentioned above. As N_2H^+ is destroyed by CO, the $\text{C}^{18}\text{O}/\text{N}_2\text{H}^+$ flux ratio is useful to constrain the CO abundance in the warm molecular layer (Trapman et al. 2022), if N_2 is not depleted significantly in contrast to CO.

Theoretically, the elemental abundance of nitrogen in the warm molecular layer can be reduced as well as that of carbon. CO and N_2 have similar volatility; laboratory experiments showed that the binding energy of N_2 is slightly lower than that of CO, and their sublimation temperatures should be within a few degrees of each other (Fayolle et al. 2016). Then, the N_2 abundance in the warm molecular layer can be reduced by the vertical cold finger effect like CO. In addition, the chemical conversion of N_2 to less volatile species (NH_3) driven by cosmic-rays/X-rays can occur after significant CO depletion (when the CO abundance becomes lower than $\sim 10^{-5}$; Furuya & Aikawa 2014).

For quantitative understanding of the evolution of C/N/O elemental abundances in disks, models, that consider both gas-ice chemistry and the vertical cold finger effect are required. Several previous studies have investigated detailed gas-ice chemistry in turbulent disks (e.g., Semenov & Wiebe 2011; Furuya et al. 2013; Furuya & Aikawa 2014). In these studies, however, dust grains were assumed to be dynamically well coupled with gas, and therefore the vertical cold finger effect was not included. Other studies focused only on carbon and oxygen, and chemical processes other than adsorption and desorption of molecules were not considered (Xu et al. 2017; Krijt et al. 2018). Krijt et al. (2020) combined the dust evolution and grain surface chemistry of carbon and oxygen driven by cosmic rays, but ignored the chemistry driven by stellar UV photons; as growth and settling of dust grains proceed, UV photons penetrate deeper into the disks, driving chemistry induced by UV photons (e.g., Akimkin et al. 2013; Van Clepper et al. 2022).

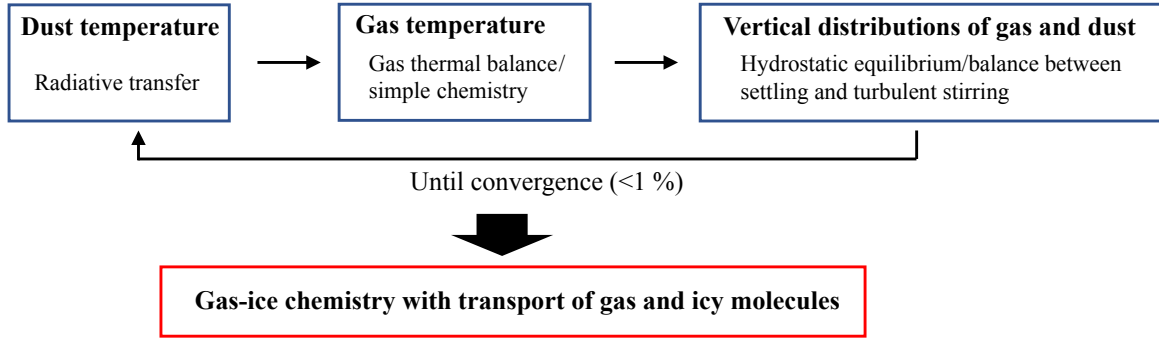


Figure 1. An outline of the modeling processes.

In this study, we investigate the time evolution of carbon-, nitrogen-, and oxygen-bearing species in a disk, considering the vertical cold finger effect and gas-ice chemistry, which includes the chemistry driven by stellar UV/X-rays and the galactic cosmic rays. The rest of this paper is organized as follows. Our numerical model is described in Section 2, and the numerical results are presented in Section 3. We discuss the timescale of elemental depletion, the temporal evolution of column densities of gas-phase species, and the midplane ice composition in Section 4. Our findings are summarized in Section 5.

2. MODEL

2.1. Numerical setup

Figure 1 shows an outline of our modeling processes. We first obtain the self-consistent solution of the density and temperature profiles of the gas and dust in the vertical direction of a disk, irradiated by stellar UV and X-rays. The gas surface density profile in the disk is taken from the TW Hya disk model developed in Cleeves et al. (2015) with the global dust-to-gas mass ratio of 0.01. The size distribution of dust in an entire disk follows a power law with an index of -3.5 with minimum (a_{\min}) and maximum radii (a_{\max}) of $0.1 \mu\text{m}$ and 1 mm , respectively. The dust size distribution is discretized into 50 logarithmically spaced bins.

Dust temperature is obtained from the radiative equilibrium using RADMC-3D code (Dullemond et al. 2012). Gas temperature is obtained by solving the steady-state balance between heating and cooling, considering simplified chemistry (Lee et al. 2021). Gas density distribution is determined from the hydrostatic equilibrium, while the distribution of dust with different radius is obtained by solving the steady-state balance between settling and turbulent stirring (e.g., Takeuchi & Lin 2002). Our vertical gas distribution is different from that in Cleeves et al. (2015), which was calculated assuming a Gaussian profile and the parametric gas scale height. We have confirmed that the degree of carbon and nitrogen depletion discussed in Section

3 does not change significantly whether using the vertical gas distribution from the hydrostatic equilibrium or the parametric distribution in Cleeves et al. (2015). The dust settling velocity and the diffusion coefficient for turbulent stirring are given later in this section.

The input stellar spectrum is composed of the observed UV spectrum of TW Hya (Dionatos et al. 2019), added to a Black body component with the effective temperature of 4110 K (Andrews et al. 2012). As our model is one-dimensional plane-parallel, the stellar flux at a radius R from the star is assumed to be absorbed at the surface of the disk and half of the flux diffuses into the vertical direction towards the midplane. The stellar flux at wavelength ν at the surface of the disk ($z_s(R) = 0.8R$ in our models) is given by

$$F(\nu, R) = \frac{1}{2} \frac{L_*(\nu)}{R^2 + z_s(R)^2}, \quad (1)$$

where $L_*(\nu)$ is the stellar spectrum. The stellar flux at each height z is calculated by RADMC-3D (Dullemond et al. 2012). The dust opacity for UV and longer wavelengths is calculated with `dsharp_opac` package from Birnstiel et al. (2018), assuming the dust composition listed in their Table 1. In addition to dust, we consider polycyclic aromatic hydrocarbons (PAHs) as a source of UV opacity (Weingartner & Draine 2001) and gas heating. We assume that a PAH radius of $\sim 5 \text{ \AA}$ (Weingartner & Draine 2001) and PAHs are always dynamically coupled with gas. The average Galactic PAH-to-dust mass ratio is 4.6 % (Draine & Li 2007), while the PAH abundance in disks is lower than that value by a factor of 10-100 (Geers et al. 2006). In our models, PAH-to-dust mass ratio in an entire disk is assumed to be 0.05 %, i.e., 100 times lower than the Galactic average value. X-ray ionization rate is calculated by the analytical formula (Igea & Glassgold 1999; Bai & Goodman 2009), with the stellar X-ray luminosity of $10^{30} \text{ erg s}^{-1}$. The non-attenuated cosmic-ray (CR) ionization rate is set to be 10^{-18} s^{-1} and the CR ionization rate of each disk position is calculated with the at-

tenuation column of 96 g cm^{-2} (Umebayashi & Nakano 1981).

Next, we solve gas and ice chemistry, considering the vertical transport of gas and ice, under the physical conditions obtained in the first step:

$$\frac{\partial n_i}{\partial t} + \frac{\partial(n_i V_T)}{\partial z} - \frac{\partial \phi_i}{\partial z} = P_i - L_i, \quad (2)$$

$$\phi_i = -n_H \frac{D_z}{S_c} \frac{\partial}{\partial z} \left(\frac{n_i}{n_H} \right), \quad (3)$$

where n_i is the number density of species i , and z is the height from the midplane. P_i and L_i represent the production rate and the loss rate, respectively, of species i by chemical reactions (see Section 2.2). The second term in the left-hand side of Equation (2) describes the vertical settling of dust, while the third term describes the turbulent diffusion. The dust settling velocity is $V_T = -\Omega_K \tau_s z$, where Ω_K is the Keplerian orbital frequency (Nakagawa et al. 1981). Assuming Epstein regime, the dimensionless stopping time τ_s is defined as $\tau_s = \rho_{\text{int}} \Omega_K a / \rho_g c_s$, where ρ_{int} is the internal density of dust (1.68 g cm^{-3}), a is the radius of dust, ρ_g is the mass density of gas, and c_s is the local sound velocity. The diffusion coefficient is parameterized as $D_z = \alpha c_s^2 / \Omega_K$ (Shakura & Sunyaev 1973), where α is assumed to be 10^{-3} in this study, unless otherwise stated. The Schmidt number, S_c , describes the strength of coupling between gas and dust and is given by $1 + \tau_s^2$ (Youdin & Lithwick 2007). For gas phase species, $V_T = 0$ and $S_c = 1$.

For the numerical integration of Equation 2, the first order operator splitting method is employed; we first integrate the equation between times t and $t + \Delta t$ without the source terms of chemical reactions. Next, we integrate the equation without the transport terms (i.e., only with the terms of chemical reactions) between times t and $t + \Delta t$ at each height z . In the time integration of the chemical reaction terms, we re-bin the dust size distribution into 8 bins (that is, icy species on 8 different dust populations are distinguished from each other) to shorten the computational time. The dust sizes for each of the 8 dust populations are $(a_{\text{min},j}, a_{\text{max},j}) = (0.10 \text{ } \mu\text{m}, 0.32 \text{ } \mu\text{m}), (0.32 \text{ } \mu\text{m}, 1.0 \text{ } \mu\text{m}), (1.0 \text{ } \mu\text{m}, 3.2 \text{ } \mu\text{m}), (3.2 \text{ } \mu\text{m}, 10 \text{ } \mu\text{m}), (10 \text{ } \mu\text{m}, 32 \text{ } \mu\text{m}), (32 \text{ } \mu\text{m}, 100 \text{ } \mu\text{m}), (100 \text{ } \mu\text{m}, 320 \text{ } \mu\text{m}),$ and $(320 \text{ } \mu\text{m}, 1 \text{ mm})$, where $a_{\text{max},j}$ and $a_{\text{min},j}$ are the maximum and minimum radius for each dust bin, respectively. Even if we used the larger number (e.g., 12) of dust bins for re-binning, numerical results presented in Section 3 remained almost unchanged.

The averaged radius (\bar{a}_j) of each dust bin for calculations of the chemistry are defined as follows

(Vasyunin et al. 2011):

$$\bar{a}_j(z) = \frac{\int_{a_{\text{min},j}}^{a_{\text{max},j}} a^3 f(a, z) da}{\int_{a_{\text{min},j}}^{a_{\text{max},j}} a^2 f(a, z) da}, \quad (4)$$

where f is the number density of grains with size between a and $a + da$. Dividing the total mass of each dust population per unit volume ($\rho_d(a_j)$) by the mean mass of one dust grain ($4\pi \bar{a}_j^3 \rho_{\text{int}}/3$), we can obtain the number of grains with the averaged radius of \bar{a}_j per unit volume. The temperature for each dust bin (\bar{T}_d) is defined by the area-weighted average temperature (Gavino et al. 2021), because the rate coefficients of gas-dust interactions are proportional to the surface area in general:

$$\bar{T}_d(\bar{a}_j, z) = \frac{\int_{a_{\text{min},j}}^{a_{\text{max},j}} T_d(a, z) a^2 f(a, z) da}{\int_{a_{\text{min},j}}^{a_{\text{max},j}} a^2 f(a, z) da}. \quad (5)$$

2.2. Chemical reaction network

The chemical network used in this work is based on that in Furuya & Aikawa (2014), which includes gas-phase reactions, interaction between gas and (icy) grain surfaces, and grain surface reactions. UV photodissociation/photoionization rates are calculated by convolving the local radiation field and the photodissociation/photoionization cross sections (Heays et al. 2017). The self-shielding and mutual shielding factors for the photodissociation of H_2 and CO are taken from Visser et al. (2009). Shielding factors for N_2 photodissociation are taken from Li et al. (2013). The binding energies of CO , CO_2 , H_2O , and N_2 are set at 1150 K, 2600 K, 5700 K, and 1000 K, respectively.

2.3. Initial compositions

Initially, we assume spatially uniform volatile elemental abundances throughout the disk. Our underlying initial elemental abundances for $\text{H}:\text{He}:\text{C}:\text{N}:\text{O}:\text{Na}:\text{Mg}:\text{Si}:\text{S}:\text{Fe}$ are $1.00:9.75(-2):1.00(-4):6.00(-5):2.20(-4):2.25(-9):1.09(-8):9.74(-9):9.14(-8):2.74(-9)$, respectively, where $a(-b)$ means $a \times 10^{-b}$. Then the initial elemental $[\text{C}/\text{N}]$ and $[\text{C}/\text{O}]$ ratios are ~ 2 and ~ 0.5 , respectively. For initial molecular abundances, we assume that all hydrogen is in H_2 , all carbon is in CO , the remaining oxygen is in H_2O , and all nitrogen is in N_2 . The other elements are assumed to exist as either atoms or atomic ions in the gas phase. All CO and N_2 are assumed to be initially present in the gas phase. We determine the initial partitioning of H_2O among ice mantles of 8 different dust populations as follows. All H_2O is assumed to be present in ice mantles, and the number density of H_2O ice on each dust population are assumed to scale with $\rho_d(\bar{a}_j, z) / \sum_k \rho_d(\bar{a}_k, z)$,

i.e., larger sized dust grains have the larger amount of H_2O ice.

Our two-step approach assumes that large dust grains are already settled and the depletion of elemental carbon, nitrogen, and oxygen in the disk upper layers have not occurred yet at the beginning of our simulations. The first assumption would be verified, because observations of Class 0/I sources have found that their inner (<1000 au) dense regions already contain mm-sized dust grains (e.g., Miotello et al. 2014; Harsono et al. 2018; Galametz et al. 2019). In addition, the presence of dust ring structures observed in some Class 0/I disks may indicate that dust coagulation and settling have already started in the young disks (e.g., Sheehan & Eisner 2018; Nakatani et al. 2020; Ohashi et al. 2021). The second assumption would be justified as well, at least for carbon and nitrogen; Class 0/I disks are warmer than Class II disks (i.e., the vertical cold finger effect is less efficient) with no signs of CO freeze-out in the inner ~ 100 au (van 't Hoff et al. 2020) and with the CO abundance close to the canonical value (Zhang et al. 2020). As N_2 is more volatile than CO, it would be reasonable to assume N_2 is entirely present in the gas phase.

The situation for water (i.e., oxygen) is less clear. The H_2^{18}O emission has been detected in the inner warm ($\gtrsim 100$ K) regions (inner envelope and/or a disk), where water ice has sublimated, of several Class 0 sources at spatial scales of 100 au (Persson et al. 2012; Jensen et al. 2019). Harsono et al. (2020) reported non-detection of H_2^{18}O emission toward Class I disks at scales of 100 au, possibly because abundant large (mm-sized or even larger) dust grains suppress the emission from inner warm disk regions. Theoretically speaking, one can consider two extreme scenarios about water in Class 0/I disks. In one scenario, due to thermal desorption and/or photodesorption of water ice, followed by photodissociation of water in the gas phase, water ice on dust grains are uncovered in the upper layers of Class 0/I disks (still, water ice can exist close to the midplane). As a result, dust coagulation and settling would not cause the depletion of volatile oxygen in the disk upper layers. In this case, the volatile oxygen abundance would be uniformly $\sim 10^{-4}$ in Class 0/I disks (oxygen in CO is not counted here). In another scenario, both thermal desorption and photodesorption are negligible, and coagulation and settling of dust covered by water ice cause the depletion of volatile oxygen in the disk upper layers. In this case, the volatile oxygen abundance scales with the local dust-to-gas mass ratio in Class 0/I disks. Reality would be somewhere between the two extremes, depending on stellar properties and disk physical structures. The former scenario is assumed in our fiducial

models, while the latter scenario is discussed in Section 4.4.

3. RESULTS

3.1. Vertical distributions of molecular abundances

Figures 2 and 3 show the vertical physical structure of the disk at $R = 20$ au (inside the CO snowline) and $R = 80$ au (outside the CO snowline) as functions of z/R . Larger dust grains tend to settle closer to the midplane (e.g., Dullemond & Dominik 2004), and the dust mass is dominated by population with the largest size ($\lesssim 1$ mm). However, even at the disk midplane, the total cross section of dust, which is relevant with the rates of gas-dust interaction, is dominated by the population with the smallest size ($< 1 \mu\text{m}$). The dust temperature of larger dust grains is colder than that of smaller ones in the disk upper layers ($\gtrsim 0.1 z/R$), reflecting the different wavelength-dependency of the opacity of different sized dust grains (e.g., Wolf 2003). Near the disk midplane, where even the sub-mm radiation becomes optically thick, the dust temperature is independent of its size. As discussed in the Appendix A, the size-dependent dust temperature is essentially important for the vertical cold finger effect. Stellar far ultraviolet (FUV) radiation starts to be attenuated at $z/R \sim 0.2$, above which the gas temperature is higher than the dust temperatures. FUV radiation can penetrate relatively deep into the disk; $\chi > 1$ even at $z/R \sim 0.1$, where χ is the wavelength-integrated FUV flux normalized by the Draine field (Draine 1978).

The top panels in Figure 4 show the abundances of selected species as functions of z/R at $R = 20$ au and $R = 80$ au at 1 Myr in the model without any transport processes (i.e., only chemical reactions are considered; hereafter called static model). At $R = 20$ au, gas-phase CO is abundant with the abundance of $\sim 10^{-4}$ except at $z/R \gtrsim 0.25$, where CO is efficiently dissociated by stellar UV photons. At $z/R \sim 0.1$, where stellar UV photons are partly attenuated ($\chi \sim 1$), CO_2 ice is formed by the surface two-body reaction between CO ice and OH ice, the latter of which is formed by photodissociation of H_2O ice (e.g., Watanabe & Kouchi 2002; Ioppolo et al. 2009; Oba et al. 2010; Noble et al. 2011; Eistrup et al. 2016; Bosman et al. 2018; Ruaud & Gorti 2019; Ruaud et al. 2022). Above $z/R \sim 0.1$, the stellar UV radiation is too strong, and CO_2 and H_2O ices are destroyed and not present abundantly. The CO_2 -rich regions also appear at $R = 80$ au between the CO-ice rich and CO-gas rich regions ($z/R \sim 0.1$ – 0.2). The conversion of CO into CO_2 is driven by stellar UV photons, and the cosmic-ray/X-ray induced UV photons are less

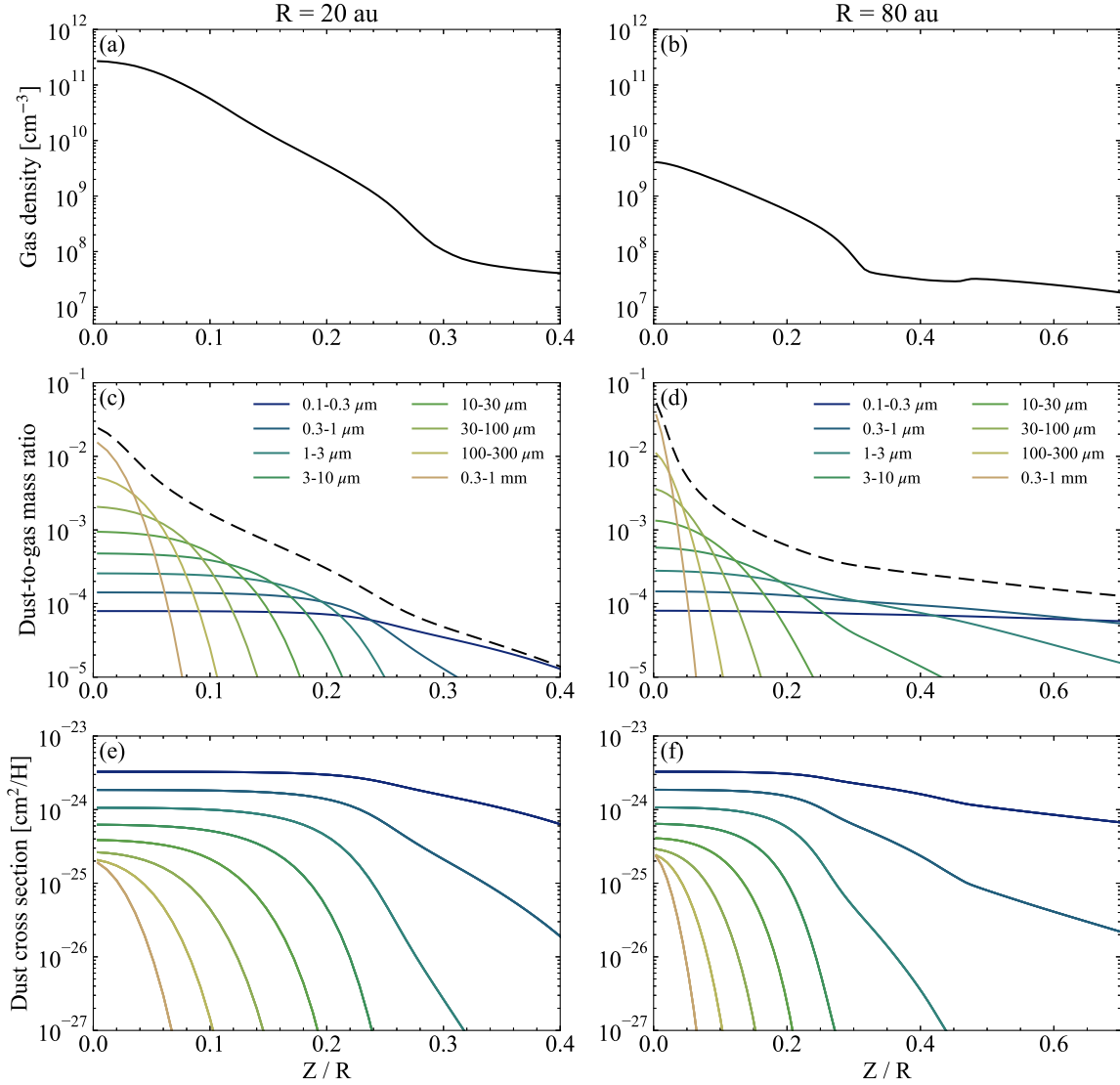


Figure 2. Vertical physical structures of a disk at $R = 20$ au (left panels) and 80 au (right panels) as functions of Z/R . (a, b) Gas density. (c, d) Dust-to-gas mass ratio for the 8 dust populations. Black dashed lines represent the sum of the dust-to-gas mass ratio for the 8 dust populations. (e, f) Total cross section for the 8 dust populations per hydrogen nuclei. For comparison, when the size of all dust grains is $0.1 \mu\text{m}$ and the dust-to-gas mass ratio is 0.01, the total cross section is $\sim 3 \times 10^{-22} \text{ cm}^2$ per hydrogen nuclei.

relevant, because the flux of the latter is lower than the former by several orders of magnitude at $z/R \sim 0.1$.

The middle panels in Figure 4 show the molecular abundances at 1 Myr in the model without surface chemistry but with the transport processes. In this model, all two-body reactions on grain surfaces and photodissociation of icy species are turned off, but adsorption of gas-phase species and thermal/non-thermal desorption of icy species are considered. At $R = 80$ au, where the dust temperatures near the midplane are low enough for the freeze-out of CO and N_2 , the gas-phase abundances of CO and N_2 become lower than their canonical values (1×10^{-4} and 3×10^{-5} , respectively) by factors of

~ 5 and ~ 3 , respectively, due to the vertical cold finger effect. The impact of the vertical cold finger effect is more significant for CO than N_2 , because of the higher binding energy of CO (1150 K) than that of N_2 (1000 K). As a result, the elemental abundances of nitrogen and carbon become similar at $R = 80$ au. At $R = 20$ au, the temperatures of all dust populations are higher than the freeze-out temperature of CO and N_2 even at the midplane. Then the cold finger effect does not work, and the gas-phase abundances of CO and N_2 in the warm molecular layers are their canonical values.

The bottom panels in Figure 4 show the molecular abundances at 1 Myr in our full model, where both

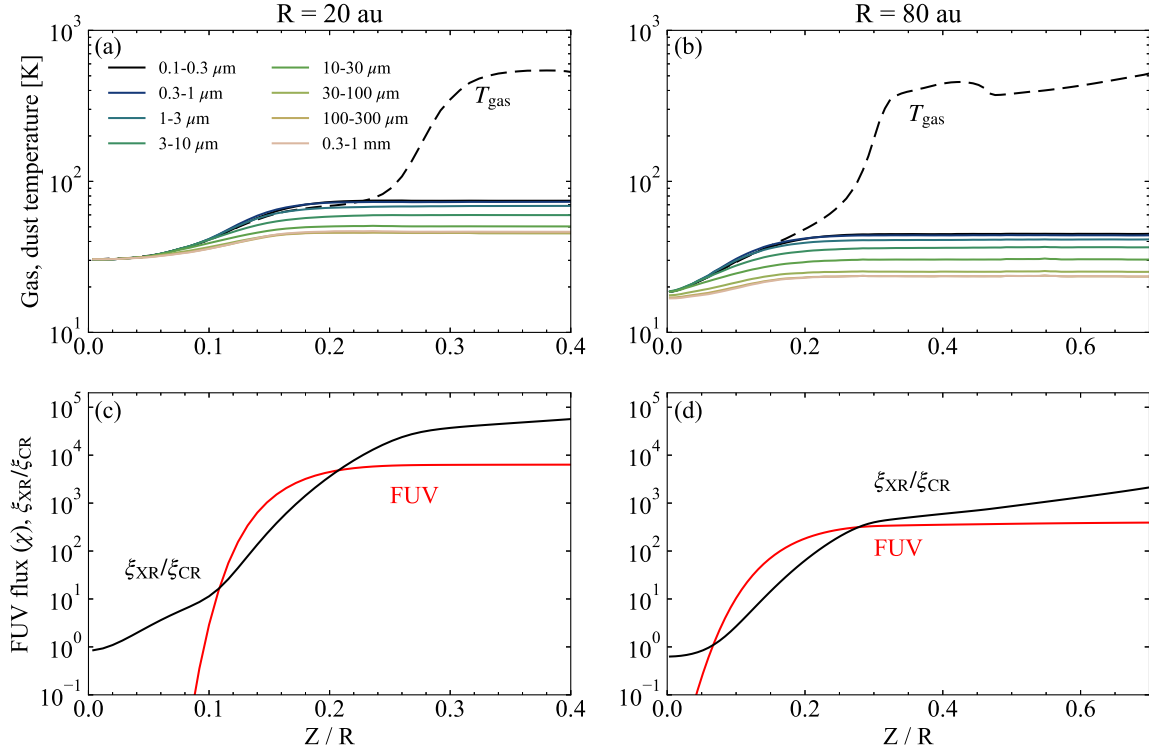


Figure 3. Similar to Figure 2, but for temperatures and UV/X-ray radiation fields. (a, b) Gas temperature (dashed black line) and dust temperature for the 8 dust populations (solid lines). (c, d) Wavelength-integrated FUV flux normalized by the Draine field ($1.6 \times 10^{-3} \text{ erg cm}^{-2} \text{ s}^{-1}$; [Draine 1978](#)) (red) and the X-ray ionization rate normalized by the non-attenuated cosmic-ray ionization rate, which is set to 10^{-18} s^{-1} (black).

transport processes and gas-ice chemistry are considered. At $R = 80$ au, CO_2 ice is the major reservoir of elemental carbon and oxygen at $z/R \lesssim 0.1$, as well as CO ice and H_2O ice. CO_2 ice is formed by the surface reaction $\text{CO} + \text{OH} \rightarrow \text{CO}_2 + \text{H}$ at $z/R \sim 0.1$ – 0.2 , where stellar UV radiation is not significantly attenuated, and transported into the midplane, where UV radiation is completely shielded, by dust settling and turbulent mixing. The source of oxygen for the CO_2 formation is H_2O ice and atomic oxygen, the latter of which is transported from the disk upper layers. N_2 does not easily react with radical species on the grain surface in contrast to CO. Owing to the much larger binding energy of CO_2 (and H_2O) compared to that of N_2 , elemental carbon and oxygen are easily locked up as ices near the midplane than nitrogen. Consequently, nitrogen becomes the third most abundant element in the gas phase after hydrogen and helium at $R = 80$ au.

At $R = 20$ au, inside the CO snowline, CO_2 ice is formed at $z/R \sim 0.1$ by the surface reaction $\text{CO} + \text{OH} \rightarrow \text{CO}_2 + \text{H}$, and transported into the midplane by dust settling and turbulent mixing like at $R = 80$ au. Because of the CO_2 formation, the gas-phase CO abundance becomes lower than the canonical value by a factor of ~ 2 at 1 Myr. The abundance of CO_2 ice remains lower than

those of CO gas and H_2O ice at $R = 20$ au. The main limiting factor of the CO_2 formation is the amount of available oxygen for the chemistry. At 80 au (outside the CO snowline), atomic O and H_2O ice at $z/R \gtrsim 0.1$ are abundant enough to convert the significant fraction of CO gas into CO_2 ice, because CO near the midplane is frozen out onto dust grains, and thus abundant only in the gas phase at $z/R \gtrsim 0.1$. H_2O ice below $z/R \lesssim 0.1$ does not contribute to the CO_2 formation, because H_2O ice is mostly on large ($\gtrsim 100 \mu\text{m}$) dust grains, which are dynamically decoupled from the gas, and because the stellar UV radiation to dissociate H_2O ice is significantly attenuated. At 20 au (inside the CO snowline), however, atomic O and H_2O ice at $z/R \gtrsim 0.1$ are not abundant enough, because CO gas is present throughout (both in the surface layer and at the midplane). As a result, the conversion of CO gas into CO_2 ice is not very efficient inside the CO snowline compared to outside the CO snowline.

Our models neglect radial drift of dust grains. As discussed in Appendix B, the size of dust grains which contributes to the grain surface chemistry efficiently is $\lesssim 100 \mu\text{m}$, and larger dust grains do not play a significant role on the chemistry. The dimensionless stopping time of $100 \mu\text{m}$ -sized dust grains is $\sim 10^{-3}$ and $\sim 5 \times 10^{-3}$ at

the midplane of $R = 20$ au and 80 au, respectively. For a $100\ \mu\text{m}$ -sized dust grain, the timescale of drifting from 80 au to 30 au (i.e., around the CO snowline) is evaluated to be $\gtrsim 1$ Myr using Eqs. 17 and 18 in Brauer et al. (2008). Then the impact of radial drift on our results on the carbon and nitrogen depletion outside the CO snowline would be not significant. Inside the CO snowline, radial drift of CO-ice mantled dust grains from the outer regions, followed by the sublimation of CO ice can enhance the CO gas abundance (e.g., Krijt et al. 2020). This effect would not be negligible, as not small amount of CO is present on large dust grains ($\gtrsim 100\ \mu\text{m}$).

3.2. Depletion factors of carbon and nitrogen

We define depletion factors of element X as

$$f_{\text{depl}}(\text{X}) = [\text{X}/\text{H}]_0 / [\text{X}/\text{H}]_{ss}, \quad (6)$$

where $[\text{X}/\text{H}]_0$ is the initial elemental abundance of X with respect to H, and $[\text{X}/\text{H}]_{ss}$ is the elemental abundance of X with respect to H in the gas above the snow surfaces of CO for carbon and N_2 for nitrogen (cf. Zhang et al. 2019; Krijt et al. 2020). Larger value of $f_{\text{depl}}(\text{X})$ means that the depletion of element X in regions above the snow surface is more significant. We define the position of the CO snow surface as the height below which multilayered CO ice can be present on at least one of the 8 dust populations. We compare the total desorption rate of CO by thermal desorption and photodesorption with its adsorption rate for each dust population, assuming the gas-phase CO abundance is 10^{-4} and grain surfaces are covered by one-monolayer of CO ice. The snow surface of CO is defined as the height above which the desorption rate of CO is greater than the adsorption rate for all dust populations. Similar definition is applied to the snow surface of N_2 . The positions of the snow surfaces are the same among different models as long as we adopt the same disk physical model.

Figure 5 shows $f_{\text{depl}}(\text{C})$ and $f_{\text{depl}}(\text{N})$ as functions of R in the static model (left panel), the model without surface chemistry (middle panel), and our full model (right model) at $t = 0.1$ Myr, 0.3 Myr, and 1 Myr. As we ran our models only at $R = 20, 30, 50, 80$, and 100 au, we cannot infer the exact radial positions of the CO and N_2 snowlines; the CO snowline is located at around 30 au, while the N_2 snowline is located at around 50 au. In the static model, $f_{\text{depl}}(\text{N})$ is almost unity (i.e., no significant depletion) regardless of R , while $f_{\text{depl}}(\text{C})$ is ~ 3 –5 well outside the CO snowline. In the model without surface chemistry, $f_{\text{depl}}(\text{C})$ is in the range of ~ 2 –20 outside the CO snowline, while it is close to unity inside the CO snowline. At $R = 50$ au, the CO snow surface

is close to the midplane compared to that at $R \geq 80$ au, leading to the lower efficiency of the vertical cold finger effect. The radial profile of $f_{\text{depl}}(\text{N})$ basically follows that of $f_{\text{depl}}(\text{C})$, and $f_{\text{depl}}(\text{C})/f_{\text{depl}}(\text{N})$ is ~ 1 –2. In the full model, $f_{\text{depl}}(\text{N})$ is similar to that in the model without surface chemistry, because nitrogen in the warm gas is depleted only by the cold finger effect of N_2 . $f_{\text{depl}}(\text{C})$ in the full model is the largest (~ 3 –30) among the three models, because of the combination of the vertical cold finger effect and the surface chemistry which converts CO into CO_2 . Consequently, $f_{\text{depl}}(\text{C})/f_{\text{depl}}(\text{N})$ can be as high as ~ 3 –5 in the full model, i.e., carbon is more depleted than nitrogen by a factor of $\gtrsim 3$ outside the CO snowline, leading to higher abundance of gas-phase nitrogen than that of gas-phase carbon. We also run some additional models to explore the parameter dependence of $f_{\text{depl}}(\text{C})$ and $f_{\text{depl}}(\text{N})$, varying ξ_{CR} , a_{max} , and a_{min} (see the Appendix C in details). We confirmed that these parameters did not affect our qualitative chemical results. Then, the combination of the cold finger effect and the grain surface chemistry results in larger depletion of carbon than nitrogen outside the CO snowline within 1 Myr once the dust grains have settled towards the midplane, making nitrogen the third most abundant element in the gas phase after hydrogen and helium. Our full model is consistent with the observations toward the IM Lup disk with the age of 0.5–1 Myr, where carbon and oxygen are depleted compared to the ISM abundance by a factor of ~ 20 or even larger, whereas nitrogen depletion is less significant (Cleeves et al. 2018).

4. DISCUSSION

4.1. Timescale of elemental depletion: UV driven chemistry versus CR driven chemistry

In our full model, outside the midplane CO snowline, the volatile carbon abundance in the warm molecular layer can be reduced by a factor of more than 10 within 1 Myr due to the combination of the vertical cold finger effect and the chemical conversion of CO into CO_2 ice driven by stellar UV photons. On the other hand, the nitrogen abundance in the warm molecular layer is reduced solely due to the vertical cold finger effect of N_2 . Here we discuss which processes determine the evolutionary timescale of the elemental abundances in the warm molecular layer.

When the turbulent mixing is switched off (the static model), the chemical conversion of CO into CO_2 ice occurs only in the limited regions ($z/R \sim 0.1$ –0.2). In the full model, however, CO_2 ice formed at $z/R \sim 0.1$ –0.2 can be transported to midplane via the turbulent mixing and dust settling, while CO near the midplane and in the disk upper layers can be transported to the re-

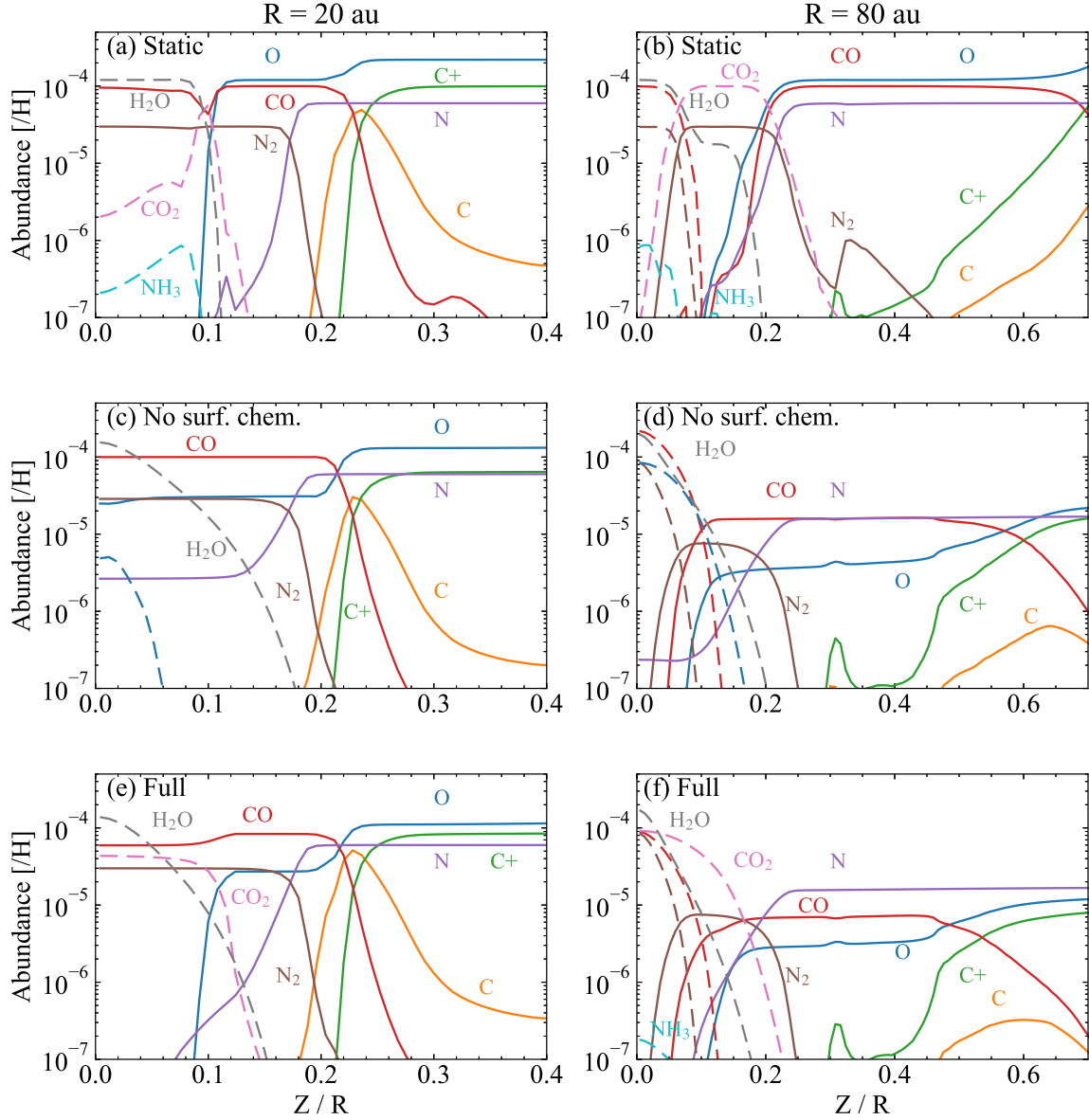


Figure 4. Vertical distributions of the abundances of selected species with respect to hydrogen nuclei at $R = 20$ au (left panels) and 80 au (right panels) at 1 Myr. Top, middle, and bottom panels show the static model (i.e., only chemistry is considered), the model without grain surface chemistry, and our full model, respectively. Gas phase species are shown by solid lines, while icy species are shown by dashed lines. For icy species, the total abundances (i.e., the sum of the ice abundances on 8 dust populations) are shown.

gions at $z/R \sim 0.1$ – 0.2 via the turbulent mixing. Then, the CO_2 -rich regions are expanded with time. The timescale of this process is limited by mixing, because the timescale of the freeze-out of CO and atomic O onto dust grains (τ_{fr}) and that of the chemistry driven by stellar UV photons (τ_{phd}) are shorter than the mixing timescale. The turbulent mixing timescale is given by $\tau_{\text{mix}} \sim (0.1r)^2/D_z$. For example, τ_{mix} is $\sim 3 \times 10^4$ yr at $R = 20$ au, $\sim 8 \times 10^4$ yr at 50 au, and $\sim 2 \times 10^5$ yr at 100 au in our models, where α is assumed to be 10^{-3} . The

freeze-out timescale τ_{fr} is given by

$$\tau_{\text{fr}} \approx 3000 \left(\frac{10^{-24} \text{ cm}^2/\text{H}}{\sigma_d} \right) \left(\frac{10^9 \text{ cm}^{-3}}{n_{\text{H}}} \right) \text{ yr}, \quad (7)$$

where σ_d is the total dust cross section per hydrogen nuclei, and n_{H} is the number density of hydrogen nuclei. As OH ice is produced by H_2O ice photodissociation, τ_{phd} is given by

$$\tau_{\text{phd}} \approx 100(\chi/1)^{-1} \text{ yr}. \quad (8)$$

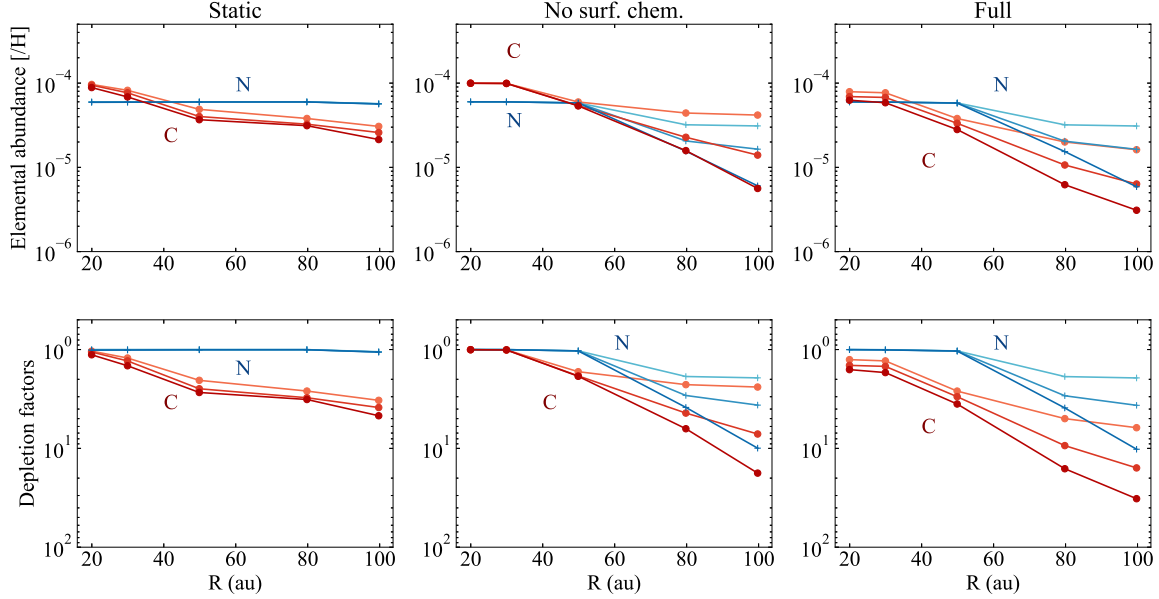


Figure 5. Abundances (top) and depletion factors (bottom) of elemental carbon (red lines) and nitrogen (blue lines) above the snow surfaces of CO and N₂, respectively, in the static model (left), the model without grain surface chemistry (middle), and in the full model (right) at 0.1 Myr, 0.3 Myr, and 1 Myr. The depletion factors monotonically increase with time.

Cosmic-ray/X-ray induced UV photons are less important than the stellar UV; the FUV flux induced by cosmic rays in the dense molecular cloud core environment, where ξ is $\sim 10^{-17} \text{ s}^{-1}$, is $\sim 10^4 \text{ photons cm}^{-2} \text{ s}^{-1}$. As $\chi = 1$ corresponds to the FUV flux of $\sim 10^8 \text{ photons cm}^{-2} \text{ s}^{-1}$, the cosmic-ray/X-ray induced UV photons are negligible unless $\xi \gtrsim 10^{-14} \text{ s}^{-1}$ (see Figure 2). Then τ_{mix} is much shorter than τ_{fr} and τ_{phd} .

On the other hand, there are many previous modeling studies which show that CO is converted into less volatile species via the chemistry driven by cosmic-rays and X-rays (e.g., Bergin et al. 2014; Furuya & Aikawa 2014). In brief, CO is destroyed by He^+ to produce C^+ and atomic O, which are eventually locked up in icy CO₂, icy CH₄, and icy carbon-chain molecules. As these molecules are much less volatile than CO, they are present in ice mantles even inside the CO snowline. As the rate-limiting step of the CO gas reprocessing chemistry is the ionization of He by cosmic-rays/X-rays to produce He^+ , the timescale is given by

$$\begin{aligned} \tau_{\text{CRchem}} &\approx \frac{x_{\text{CO}}}{\xi_{\text{He}} x_{\text{He}}} \\ &\approx 2 \times 10^7 \left(\frac{x_{\text{CO}}}{1 \times 10^{-4}} \right) \left(\frac{\xi_{\text{He}}}{5 \times 10^{-19} \text{ s}^{-1}} \right)^{-1} \text{ yr}, \end{aligned} \quad (9)$$

where x_i is the abundance of species i , and ξ_{He} is the ionization rate of He atom (Furuya & Aikawa 2014), which is a half of the ionization rate of H₂. Then τ_{CRchem} is much larger than τ_{phd} and τ_{mix} . N₂ can also be con-

verted into less volatile species (NH₃ ice) by the following pathway (Willacy 2007; Furuya & Aikawa 2014): $\text{N}_2 \xrightarrow{\text{H}_3^+} \text{N}_2\text{H}^+ \xrightarrow{\text{e}^-} \text{NH}$. Once NH is formed, it is adsorbed onto dust grains, followed by subsequent hydrogenation to form NH₃ ice. The timescale of the N₂ conversion into NH₃ ice is slightly longer than τ_{CRchem} , as it occurs only after the significant depletion of CO gas (when the CO abundance is lower than $\sim 10^{-5}$); otherwise N_2H^+ is destroyed by CO and N₂ is reformed (Furuya & Aikawa 2014). τ_{CRchem} is much longer than τ_{phd} and τ_{mix} , and thus the chemistry driven by cosmic-rays (and X-rays) are less important than that driven by stellar UV photons. Even if the higher value for ξ_{CR} of 10^{-16} s^{-1} is assumed, the above conclusion holds, because τ_{CRchem} is still larger than τ_{fr} , τ_{phd} , and τ_{mix} . Indeed, the depletion factors of carbon and nitrogen do not change significantly between the model with $\xi_{\text{CR}} = 10^{-18} \text{ s}^{-1}$ and that with $\xi_{\text{CR}} = 10^{-16} \text{ s}^{-1}$ (see Appendix C).

4.2. Dependence on the strength of turbulence

In our models presented so far, the α parameter for the vertical diffusion coefficient is assumed to be 10^{-3} . As discussed in Section 4.1, the timescale of carbon and nitrogen depletion is mostly determined by the turbulent mixing timescale, and thus the α parameter should affect the timescale and the degrees of the carbon and nitrogen depletion at given time. Recent observational studies have put constraints on the strength of the turbulence in the warm molecular layers for some disks on the basis of the molecular line observations. Flaherty et al. (2020)

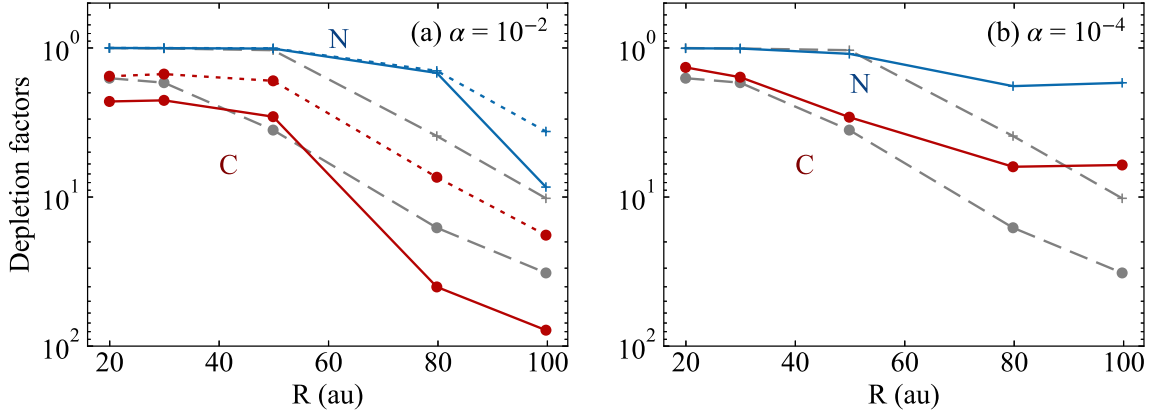


Figure 6. Depletion factors of elemental carbon (red solid lines) and nitrogen (blue solid lines) in the full model with $\alpha = 10^{-2}$ (left) and with $\alpha = 10^{-4}$ (right) at 1 Myr. Dashed gray lines represent the depletion factors in the model with $\alpha = 10^{-3}$ at 1 Myr for comparisons. The dotted lines in the left panel shows the depletion factors in the model with $\alpha = 10^{-2}$ at 0.1 Myr.

constrained the non-thermal gas motion (δv) in disks around DM Tau, MWC 480, and V4046 Sgr, based on the ^{12}CO 2–1 observations and parametric disk models. Converting δv to α by $\alpha = (\delta v/c_s)^2$, they found that $\alpha \sim 8 \times 10^{-2}$ for the DM Tau disk, $\alpha < 3 \times 10^{-3}$ for the MWC 480 disk, and $\alpha < 1 \times 10^{-2}$ for the V4046 Sgr disk in the gas traced by ^{12}CO 2–1, i.e., not the disk midplane. Similar observational studies toward the disks around TW Hya and HD 162936 indicate $\alpha < 7 \times 10^{-3}$ and $\alpha < 3 \times 10^{-3}$, respectively (Teague et al. 2016; Flaherty et al. 2017, 2018).

These observational studies seem to indicate that the strength of the turbulence is not strong ($\alpha \lesssim 10^{-3}$) in disks in general, but the turbulence is strong ($\alpha \gtrsim 10^{-2}$) in some disks. To explore the impact of the α value on the model results, we recalculated the entire modeling processes (Figure 1) with $\alpha = 10^{-2}$ and $\alpha = 10^{-4}$ as the value of α parameter also affects the disk physical conditions. Figure 6 shows $f_{\text{depl}}(\text{C})$ and $f_{\text{depl}}(\text{N})$ in full models with $\alpha = 10^{-2}$ (left panel) and $\alpha = 10^{-4}$ (right panel). As the mixing timescale is inversely proportional to α , $f_{\text{depl}}(\text{C})$ already reaches ~ 10 at 0.1 Myr at $R \geq 80$ au in the model with $\alpha = 10^{-2}$. Both $f_{\text{depl}}(\text{C})$ and $f_{\text{depl}}(\text{N})$ reach the steady state values within 1 Myr in the model with $\alpha = 10^{-2}$. In the model with $\alpha = 10^{-3}$, $f_{\text{depl}}(\text{N})$ almost reaches the steady state value within 1 Myr, while $f_{\text{depl}}(\text{C})$ does not. We reran the model with $\alpha = 10^{-3}$ for 3 Myr, and confirmed that $f_{\text{depl}}(\text{C})$ reaches ~ 50 and ~ 60 at $R = 80$ au and $R = 100$ au, respectively, at 3 Myr, while $f_{\text{depl}}(\text{C})$ at $R \leq 50$ au almost reaches the steady state value within 1 Myr. In the model with $\alpha = 10^{-4}$, the depletion factors are less than 10 even at 1 Myr, because of the long mixing timescale (e.g., longer than 1 Myr at $R \gtrsim 50$ au). Therefore, relatively large value of α ($\gtrsim 10^{-3}$) is favorable for the significant de-

pletion of carbon and making the warm molecular layer enriched in nitrogen relative to carbon within 1 Myr.

On the other hand, Anderson et al. (2019) found that $\text{N}_2\text{H}^+/\text{CO}$ flux ratio is higher in 5–10 Myr disks than younger disks with the age of < 2 Myr. If this trend primary traces the evolution of volatile elemental abundances, the depletion of carbon should continue in 5–10 Myr. Because time it takes for the depletion factors reach steady state is shorter for higher α value, our model with $\alpha = 10^{-4}$ or 10^{-3} may be more consistent with the finding by Anderson et al. (2019) rather than the model with $\alpha = 10^{-2}$. Taken together, to explain the observed CO (or carbon) depletion timescale by our models, the reasonable value of α is $\sim 10^{-3}$.

4.3. Column densities of gas-phase molecules

Here we discuss how the column densities of gas-phase species evolve with time in our full model with $\alpha = 10^{-3}$. Figure 7 shows the column densities of CO and N_2 , their protonated species (HCO^+ and N_2H^+), and the probe of the elemental carbon-to-oxygen ratio in the gas-phase (hereafter $[\text{C}/\text{O}]_{\text{gas}}$; C_2H and HCN) at $t = 0.1, 0.3, 1$ Myr, and 3 Myr. For comparisons, we ran an additional static model, where grain surface chemistry, except for desorption and adsorption processes, was turned off (i.e., there is no depletion of carbon, oxygen, and nitrogen in the warm molecular layers). The molecular column densities predicted by this additional model at 1 Myr is shown by black dashed lines in the figure.

The column densities of CO and HCO^+ decrease with time, reflecting the gradual loss of CO from the warm molecular layer via the combination of the chemical conversion of CO and the vertical cold finger effect. The N_2 column density decreases with time at > 50 au, due to the vertical cold finger effect only. The column density of N_2 is larger than that of CO, indicating that N_2 is the

second most abundant molecule in the gas-phase. The column densities of N_2 decrease with time, whereas the N_2H^+ column density increases slightly with time rather than decreased. As N_2H^+ is destroyed by CO, the decrease of the gas-phase CO abundance leads to the enhanced N_2H^+ abundance (e.g., Aikawa et al. 2015), canceling the decrease of the gas-phase N_2 abundance. As a result, the column density ratio of CO to N_2H^+ increases with time at least until 3 Myr. This result may be consistent with the observations by Anderson et al. (2019), who found that the $\text{N}_2\text{H}^+/\text{CO}$ flux ratio in 5–11 Myr old disks in Upper Sco is higher than that in younger disks with the age of <2 Myr. Trapman et al. (2022) showed that the combination of C^{18}O and N_2H^+ lines is useful to constrain disk gas mass, adopting a static thermal-chemical disk model, assuming that nitrogen is not depleted. Our results do not fully support their assumption on the non-depletion of nitrogen. However, combination of C^{18}O and N_2H^+ lines would be useful to constrain the disk gas mass, because the carbon depletion is more significant than the nitrogen depletion, and thus the $\text{N}_2\text{H}^+/\text{CO}$ ratio can be used as a probe of the carbon (CO) depletion.

C_2H is considered as a probe of $[\text{C}/\text{O}]_{\text{gas}}$, because its abundance depends on whether $[\text{C}/\text{O}]_{\text{gas}}$ is higher than unity or not (e.g., Bergin et al. 2016; Miotello et al. 2017; Bosman et al. 2021b). In our full model, the C_2H column density increases with time by a factor of ~ 10 at most, because $[\text{C}/\text{O}]_{\text{gas}}$ becomes close to, but still lower than unity both inside and outside of the CO snowline (see panels e and f of Figure 4). The HCN column density remains almost unchanged with time in our full model. The C_2H and HCN column densities in our model ($\sim 10^{12}$ – 10^{13} cm^{-2} and $\sim 10^{11}$ – 10^{13} cm^{-2} , respectively) at 1 Myr are still one or two orders of magnitude lower than that observed in the outer regions (outside of the CO snowline) of Class II disks (Bergin et al. 2016; Bergner et al. 2020a; Guzmán et al. 2021). The underestimation of the C_2H and HCN column densities in our model indicates a need for additional process to make $[\text{C}/\text{O}]_{\text{gas}}$ higher than unity.

The rationale for $0.5 \lesssim [\text{C}/\text{O}]_{\text{gas}} \lesssim 1$ both inside and outside of the CO snow line in our model is as follows. Inside the CO snowline, only the oxygen-rich species, H_2O and CO_2 , can freeze out near the midplane. Then, the gas becomes dominated by CO over time, leading to $[\text{C}/\text{O}]_{\text{gas}} \sim 1$. Outside the CO snowline, there are two CO reservoirs at $t = 0$ yr; one is the gas-phase CO in the warm molecular layer and another is the CO ice on small dust grains near the midplane. As CO is assumed to be present in the gas phase at $t = 0$ yr, it is preferentially frozen-out onto smaller grains; smaller grains

dominate dust cross section, and dust temperature does not depend on the size near the midplane. Some CO ice near the midplane is transported upward, enriching the warm molecular layers in CO. Atomic O and CO in the surface layer are consumed by the CO_2 formation at a similar rate, but this enrichment process partially cancels out the CO depletion in the surface layers. As a result, $[\text{C}/\text{O}]_{\text{gas}}$ becomes >0.5 , but does not exceed unity.

A promising process for enhancing $[\text{C}/\text{O}]_{\text{gas}}$ is the destruction of carbon grains by photoablation as proposed by Bosman et al. (2021a). The carbon abundance locked up in refractory carbon dust is $10^{-4} \times 100\Delta_{\text{d/g}}$, where $\Delta_{\text{d/g}}$ is the dust-to-gas mass ratio. To enhance $[\text{C}/\text{O}]_{\text{gas}}$ considerably (~ 2), the carbon abundance released in the gas phase should be comparable to or larger than the gas-phase carbon abundance. Then the following relation should hold, $f_{\text{depl}}(\text{C})\Delta_{\text{d/g}} \gtrsim 10^{-2}$ (Bosman et al. 2021a), assuming complete photoablation of refractory carbon dust. In our model with $\alpha = 10^{-3}$ at 1 Myr, the requirement is satisfied at $z/R \lesssim 0.2$, even if complete photoablation of carbon grains is assumed. Below $z/R \lesssim 0.1$, however, stellar UV is significantly attenuated ($\chi \ll 1$) and/or the dust temperature is too low leading to the freeze-out of gas-phase carbon. Taken together, only very limited regions ($z/R \sim 0.1$ – 0.2) might be able to become $[\text{C}/\text{O}]_{\text{gas}} > 1$ by the photoablation. Even if so, locally high $[\text{C}/\text{O}]_{\text{gas}}$ would be smeared out by turbulent mixing in relatively short timescale (e.g., $\tau_{\text{mix}} \sim 2 \times 10^5 \text{ yr}$ at $R = 100 \text{ au}$). Therefore, as noted in Van Clepper et al. (2022), carbon grain destruction may be ongoing over the course of grain growth, rather than solely after the grain growth.

4.4. Comparisons with previous studies

Krijt et al. (2020) studied the depletion of carbon and oxygen combining the dust evolution and grain surface chemistry of carbon and oxygen driven by cosmic rays, but ignored the chemistry driven by stellar UV photons. One of the most significant differences between their study and ours is that they considered the formation of pebbles from small grains in disks, while we assumed that pebbles already exist at the beginning of our simulations. In Krijt et al. (2020), the formation and the vertical settling of pebbles transport H_2O ice to the midplane. This process leads to $[\text{C}/\text{O}]_{\text{gas}} \sim 1$, because CO is much more volatile than H_2O . On the other hand, in our models, we assumed that pebbles already exist at $t = 0$ yr and the ISM-like elemental abundance throughout the disk (i.e., $[\text{C}/\text{O}]_{\text{gas}} \sim 0.5$ in the disk upper layers, where H_2O is efficiently dissociated by stellar UV photons). As noted in Section 2.3, what happens

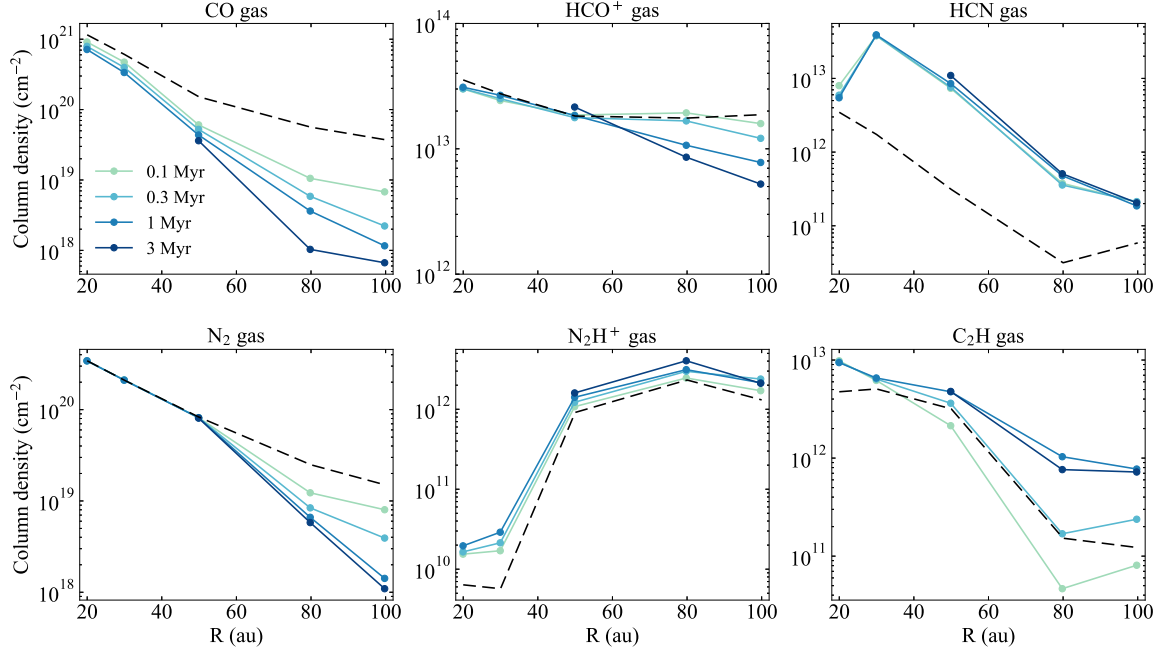


Figure 7. Radial profiles of the column densities of selected gas-phase molecules in the full model at 0.1 Myr, 0.3 Myr, 1 Myr, and 3 Myr. The column densities at 3 Myr are shown only at $R = 50, 80, 100$ au. At the inner radii, the column density almost reaches the steady state values within 1 Myr. For comparisons, black dashed lines show the column densities predicted by the static model without grain surface chemistry (i.e., no depletion of carbon and nitrogen in the warm molecular layers) at 1 Myr.

to water in young disks, where the growth of small dust grains have already started, remains unclear. The model by Krijt et al. (2020) would correspond to the scenario where the sublimation/photodesorption of water ice is negligible, and coagulation and settling of dust covered by water ice cause the depletion of volatile oxygen in the disk upper layers, because their model did not consider the chemistry induced by stellar UV and the disk is cold. Our model corresponds to another extreme scenario where water ice on dust grains are uncovered due to thermal desorption and/or photodesorption of water ice in the disk upper layers, and dust coagulation and settling do not cause the depletion of volatile oxygen in the disk upper layers. Reality would be somewhere between the two extremes, depending on stellar properties and disk physical structures. Note that the oxygen abundance in the disk upper layers would also be related to the photoablation of carbon grain; if the photoablation occurs efficiently during the formation and settling of pebbles, H_2O ice, which covers dust grains, would be photodesorbed at the same time.

In order to check the impact of elemental oxygen abundance available for the CO_2 formation on our results, we reran our full model assuming that the initial H_2O abundance scales with the local dust-to-gas mass ratio, i.e., $10^{-4} \times (\Delta_{\text{d/g}}/10^{-2})$. In other words, the initial H_2O -to-dust mass ratio is uniform inside the disk. As $\Delta_{\text{d/g}}$ is $\sim 10^{-3}$ or lower at $z/R \gtrsim 0.1$ (see Fig. 2), the elemental

abundance of oxygen not locked up in CO is lower than that in our fiducial models by a factor of ~ 10 or even larger. We confirmed that $f_{\text{depl}}(\text{C})$ in the model with the uniform H_2O -to-dust mass ratio is between that in the fiducial full model and that in the model without grain surface chemistry (Figure 8). We also confirmed that $[\text{C}/\text{O}]_{\text{gas}}$ at 1 Myr is close to unity as in the fiducial full model. Therefore, our qualitative chemical results are not sensitive to the initial oxygen abundance.

Regarding to $[\text{C}/\text{O}]_{\text{gas}}$ at 1 Myr or later, our model predicted that $[\text{C}/\text{O}]_{\text{gas}}$ becomes larger than the initial value of ~ 0.5 , but does not exceed unity. Van Clepper et al. (2022), who combined a toy model of the pebble formation and a gas-ice astrochemical model (but surface chemistry was ignored except for hydrogenation, i.e., the CO_2 formation does not occur in their model), also predicted that $[\text{C}/\text{O}]_{\text{gas}}$ does not exceed unity. On the other hand, Krijt et al. (2020) predicted that eventually $[\text{C}/\text{O}]_{\text{gas}}$ in the warm molecular layers can become larger than unity. The difference in the predicted $[\text{C}/\text{O}]_{\text{gas}}$ can be explained by the cosmic-ray driven chemistry versus UV driven chemistry. The rationale why $[\text{C}/\text{O}]_{\text{gas}} > 1$ can be realized in Krijt et al. (2020) is that they assumed C^+ , which is produced by the destruction of CO by He^+ , is eventually locked up in CH_4 , while atomic O is locked up in H_2O and/or CO_2 . As CH_4 is more volatile than H_2O and CO_2 , it can be more easily go back to the gas phase and enhance

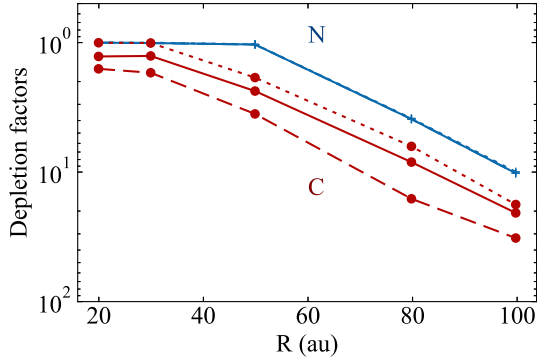


Figure 8. The depletion factors of elemental carbon (red solid line) and nitrogen (blue solid line) in the model where the initial H_2O -to-dust mass ratio is uniform inside the disk at 1 Myr. For comparisons, dashed lines and dotted lines represent the depletion factors in the fiducial full model and the model without surface chemistry. In these two models, the initial H_2O abundance is uniformly 10^{-4} .

$[\text{C}/\text{O}]_{\text{gas}}$ in the warm molecular layer. In the model by Krijt et al. (2020), the effect of stellar UV on chemistry was neglected in contrast to our models. More comprehensive simulation with dust settling, growth, and photoablation with both CR and UV driven chemistry are required for better understanding of the evolution of carbon, nitrogen, and oxygen in protoplanetary disks.

4.5. Ice compositions in the midplane

Although the main topic of this study is the gas-phase elemental abundance in the warm molecular layers, we discuss ice compositions in the disk midplane briefly, because the chemical compositions in the warm molecular layer and those in the midplane are related to each other through the turbulent mixing. We only focus on the most abundant species in the ISM ice and cometary ice, i.e., H_2O , CO , and CO_2 for C- and O-bearing species, and N_2 and NH_3 for N-bearing species.

Figure 9 shows the total abundances of selected icy molecules (i.e., the sum of the ice abundances on 8 dust populations) in the disk midplane in the static model (left), in the full model with $\alpha = 10^{-4}$ (middle), and in the full model with $\alpha = 10^{-3}$ (right) at 1 Myr. In the static model, the ice composition in the midplane is mostly determined by the assumed initial compositions and the balance between adsorption and desorption, because the timescale of the chemistry driven by cosmic-rays is longer than 1 Myr for $\xi_{\text{CR}} \lesssim 10^{-17} \text{ s}^{-1}$ (e.g., Furuya & Aikawa 2014). When the turbulent mixing is considered, we see the increases of the H_2O , CO , and N_2 abundances outside their snowlines by a factor of a few compared to the initial abundances, and the efficient formation of CO_2 ice, the abundance of which reaches

more than 10 % of the H_2O abundance within 1 Myr. Note that CO_2 ice is abundantly present in the ISM ice ($\text{CO}_2/\text{H}_2\text{O} \sim 30\%$; Boogert et al. 2015), while there is no CO_2 at the beginning of our simulations. Therefore, the impact of the vertical mixing on the abundant ($>10^{-5}$ per H) ice molecules in the disk midplane is limited, if ice in disks were inherited from the ISM ice.

On the other hand, if we look at the ice compositions of each dust population, the situation is different. Figure 10 shows radial profiles of abundances of selected icy molecules on small ($0.1\text{--}0.32 \mu\text{m}$), middle ($3.2\text{--}10 \mu\text{m}$), and large ($0.32\text{--}1 \text{ mm}$) size dust populations in the full model with $\alpha = 10^{-3}$. The ice compositions are very different, depending on dust size; for the large dust population, the ice composition is dominated by H_2O ice as assumed in the initial conditions. On the other hand, for the small- and middle-sized dust populations, the ice compositions are significantly different from the initial compositions; H_2O ice is no longer the most abundant icy species, and the $\text{CO}_2/\text{H}_2\text{O}$ abundance ratio exceeds unity. In reality, however, dust collision (coagulation and fragmentation) would average the ice mantle compositions and make the difference in the ice mantle compositions of different dust size smaller to some extent. Coupled models with dust coagulation/fragmentation and gas-ice chemistry resolving the dust size distribution are necessary for better understanding the diversity of size-dependent ice compositions.

Laboratory experiments have shown that the surface composition of dust grains affect the threshold fragmentation velocity, and thus the efficiency of collisional growth. In particular for this study, the threshold fragmentation velocity of CO_2 ice is lower than that of H_2O ice (Musiolik et al. 2016a,b). The composition of the surface of ice mantles in disks would be determined by the thermal and chemical history of icy dust grains from its formation in molecular clouds to the delivery to disks (Drozdovskaya et al. 2016; Furuya et al. 2017), and the chemistry inside disks. Although our models do not track ice layered structure, judging from the efficient formation of CO_2 ice, the surface of ice mantles of small- and middle-sized dust outside the CO snowline of disks may be covered by CO_2 ice, regardless of the initial surface composition of the ice mantles in disks. Therefore, the depletion of carbon and oxygen in the warm molecular layer may be also important for the dust coagulation/fragmentation in the disk midplane.

5. SUMMARY

We investigated the temporal evolution of elemental abundances of volatile carbon, nitrogen, and oxygen in the warm molecular layer ($\gtrsim 20 \text{ K}$) of a protoplanet-

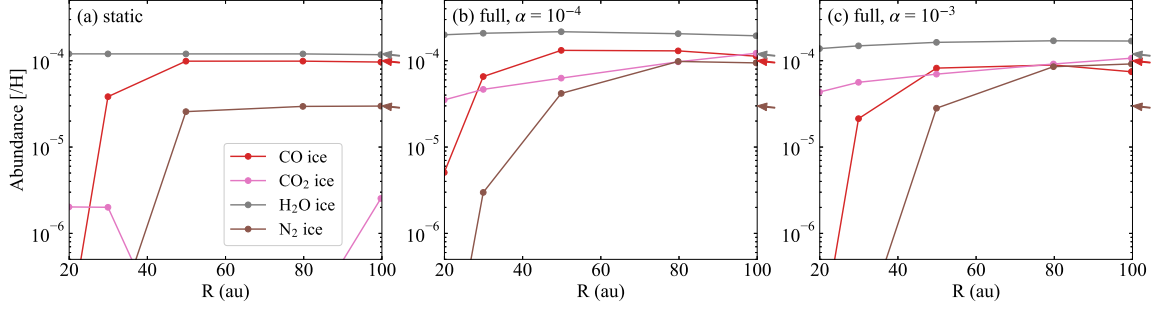


Figure 9. Radial profiles of the total abundances of selected icy molecules (i.e., the sum of the ice abundances on 8 dust populations) in the static model (left), in the full model with $\alpha = 10^{-4}$ (middle), and in the full model with $\alpha = 10^{-3}$ (right) at 1 Myr. Arrows on the right-hand margin indicate the initial abundances of H_2O , CO , and N_2 . The abundance of NH_3 is below 10^{-6} and not shown in the figure.

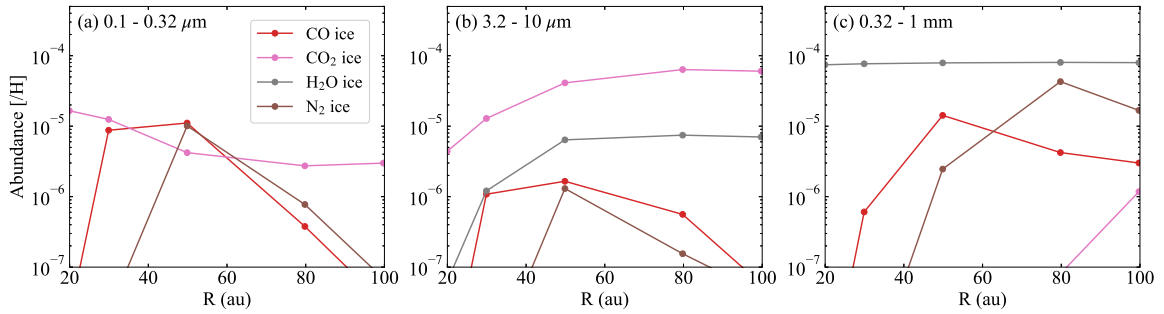


Figure 10. Radial profiles of abundances of selected icy molecules on small ($0.1\text{--}0.32\ \mu\text{m}$), middle ($3.2\text{--}10\ \mu\text{m}$), and large ($0.32\text{--}1\ \text{mm}$) sized dust populations in the full model with $\alpha = 10^{-3}$ at 1 Myr.

tary disk, considering both the vertical cold finger effect and gas-ice chemistry. We developed a one-dimensional model that incorporates dust settling, turbulent diffusion of dust and ices, as well as gas-ice chemistry including the chemistry driven by stellar UV/X-rays and the galactic cosmic rays. Our main findings are summarized as follows.

1. Outside the CO snowline, the elemental abundance of carbon in the warm molecular layer can be reduced by a factor of >10 via the combination of the vertical cold finger effect of CO and the chemical conversion of CO into CO_2 driven by stellar UV photons. On the other hand, the gaseous N_2 , the main nitrogen reservoir in the warm molecular layer, is less processed by the stellar UV driven chemistry, and exists as it is. As the binding energy of N_2 is lower than that of CO and CO_2 , the degree of nitrogen depletion in the warm molecular layer is smaller than that of carbon and oxygen, leading to higher elemental abundance of nitrogen than those of carbon and oxygen.
2. The degree of carbon and nitrogen depletion and the depletion timescale are independent of the assumed cosmic-ray ionization rate, at least, when

ξ_{CR} is less than $10^{-16}\ \text{s}^{-1}$, but depends on the strength of turbulence. In the case when the α value for the diffusion coefficient is 10^{-3} , the CO abundance in the warm molecular layers beyond the midplane CO snowline can become lower than the ISM abundance by a factors of >10 within 1 Myr. The CO abundance continues to decrease until at 3 Myr. On the other hand, the N_2 abundance reaches steady state within 1 Myr. When $\alpha = 10^{-2}$, both CO and N_2 abundance reaches state state within 1 Myr. When $\alpha = 10^{-4}$, the depletion factors of carbon and nitrogen are less than a factor of $\lesssim 5$ in 1 Myr.

3. As a result of more significant depletion of elemental carbon and oxygen than nitrogen, the $\text{N}_2\text{H}^+/\text{CO}$ column density ratio increases with time in particular for the outer disk regions (outside the N_2 snowline).
4. In our models, elemental carbon-to-oxygen ratio in the gas phase ($[\text{C}/\text{O}]_{\text{gas}}$) becomes larger than 0.5, but does not exceed unity both inside and outside of the midplane CO snowline. A promising mechanism for enhancing $[\text{C}/\text{O}]_{\text{gas}}$ would be the destruction of carbon grains by photoablation dur-

ing the course of grain growth (Section 4.3 and 4.4; see also Bosman et al. 2021b; Van Clepper et al. 2022).

5. The compositions of ice mantles at the midplane can be different, depending on dust size. Because the largest dust grains (1 mm in our models) are settled close to the midplane and the surface area per unit gas volume is small, their ice mantle compositions do not change significantly. On the other hand, smaller grains do not preserve their initial ice compositions.
6. The size dependent dust temperature (i.e., larger grains have lower temperatures, assuming the radiative equilibrium) is crucial for the efficiency of

the vertical cold finger effect (see the Appendix A in details).

ACKNOWLEDGMENTS

We thank the anonymous referee for providing thoughtful and insightful comments that helped to improve the manuscript. This work is supported in part by JSPS KAKENHI Grant numbers 18H05441, 19K03910, 20H00182, 20H05847 and 21K13967. Numerical computations were in part carried out on PC cluster at Center for Computational Astrophysics, National Astronomical Observatory of Japan.

Software: RADMC-3D (Dullemond et al. 2012), dsharp_opac (Birnstiel et al. 2018), Matplotlib (Hunter 2007)

APPENDIX

A. IMPORTANCE OF SIZE DEPENDENT DUST TEMPERATURE FOR THE VERTICAL COLD FINGER EFFECT

In previous studies of the vertical cold finger effect of CO, the temperature of a dust grain is independent of its size, that is dust grains with different sizes have the same temperature (e.g., Kama et al. 2016; Xu et al. 2017). Here, we show that this assumption can underestimate the impact of the vertical cold finger effect.

We ran the model without grain surface chemistry (see Section 3.1), employing two different assumptions for the dust temperature of the 8 dust populations. In one model, dust temperature of dust populations are calculated in the same way as in our fiducial model. Consequently, larger dust populations are colder than smaller ones. In another model, all dust populations are assumed to have the same temperature (hereafter single T_d model), and the dust temperature is assumed to be the area-weighted temperature averaged in the range between 0.1 μm and 1 mm (i.e., the entire size range in our fiducial models). The left panel of Figure A1 compares the vertical distribution of the gas-phase CO abundance in the two models at $R = 80$ au at 1 Myr. The gas-phase CO abundance is much larger (i.e., the efficiency of the vertical cold finger effect is lower) in the single T_d model compared to the fiducial model. As discussed in Kama et al. (2016), in the single T_d model, the ratio of dust cross section contributed by large dust grains which are settled below the CO snow surface to the total dust cross section (denoted as Δ_X) is the critical parameter

for determining the efficiency of the vertical cold finger effect. If Δ_X is small, most gas-phase CO adsorb onto small grains. The CO-ice coated small grains can be transported above the CO snow surface by turbulent mixing, and the CO ice can sublime into the gas phase. Thus the vertical cold finger effect is not efficient. As shown in Fig. 2, the total cross section is dominated by small grains in our model. Then the vertical cold finger effect is not efficient in the single T_d model.

However, in the fiducial model, where smaller grains have higher temperatures, the net adsorption rate (i.e., the adsorption rate of gas-phase CO minus the desorption rate of CO ice) of the large dust grains can be larger than that of the small dust grains, even if $\Delta_X \ll 1$ (see the right panel of Fig. A1). Then the single T_d model underestimates the efficiency of the vertical cold finger effect.

The vertical cold finger effect was originally introduced by an analogy of the radial cold finger effect (Stevenson & Lunine 1988; Meijerink et al. 2009). As the dust temperature is essentially the same in the disk midplane irrespective of its size, the size dependent dust temperature discussed here is not relevant for the radial cold finger effect, but is critically important for the vertical cold finger effect.

B. ROLES OF DIFFERENT SIZED DUST GRAINS IN DISK CHEMISTRY

Figures A2 and A3 show the vertical distribution of the abundances of selected icy species on the 8 dust populations at $R = 80$ au and $R = 20$ au, respectively. At

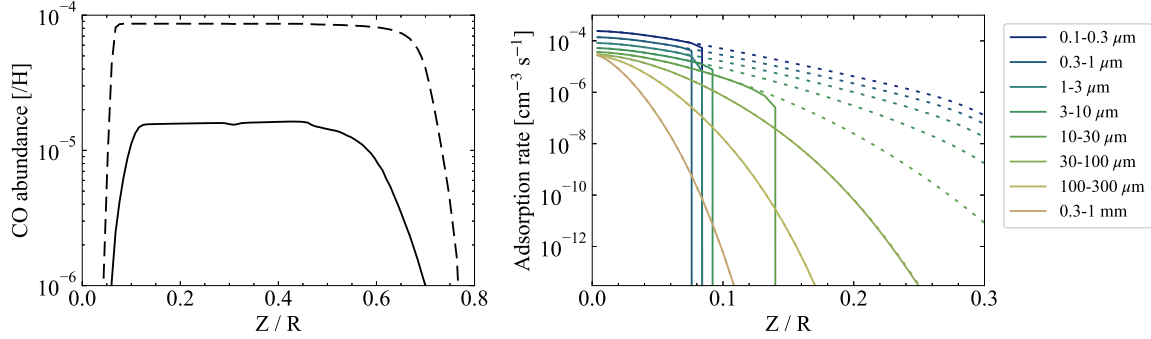


Figure A1. Left) Vertical distribution of the gas-phase CO abundance in the fiducial model (solid line) and in the single T_d model (dashed line) at $R = 80$ au and at 1 Myr. In both models, grain surface chemistry is switched off. Right) Adsorption rates of CO onto 8 dust populations in the fiducial model are shown by dotted lines, while net adsorption rates (i.e., the adsorption rate of gas-phase CO minus the desorption rate of CO ice) are shown by solid lines.

$R = 80$, the formation of CO_2 ice occurs mainly on the middle-sized grain populations ($\sim 10 \mu\text{m}$), because gas-phase CO preferentially freeze out on those populations at $z/R \sim 0.1$ (right panel of Fig. A1), where stellar UV is not fully shielded. Large dust populations ($\gtrsim 100 \mu\text{m}$) are dynamically decoupled from the gas, and elements locked up in H_2O , CO, and N_2 ices on the large dust grains do not contribute to the active chemistry at $z/R \gtrsim 0.1$.

At $R = 20$ au, on the other hand, the formation of CO_2 ice occurs mainly on small dust populations ($\sim 1 \mu\text{m}$ or less), because the dust temperatures for all dust populations are too high for the CO freeze-out, and thus dust populations with larger total cross sections (i.e., small populations) are more important for the surface chemistry. Then, the important dust size for CO_2 formation depends on the distance from the star. As at $R = 80$ au, large dust populations ($\gtrsim 100 \mu\text{m}$) are dynamically decoupled from the gas, and oxygen locked up in H_2O ice on the large dust grains do not contribute to the chemistry at $z/R \gtrsim 0.1$.

As discussed above, different sized dust grains contribute to the disk chemistry in the different ways. Disk chemical models often adopt the single grain approximation, where gas-ice chemistry is described assuming a single-grain size and temperature (see Gavino et al. 2021, and references therein). It is clear that the disk chemistry with turbulent mixing cannot be represented by models with the single grain approximation. The similar argument was made by Gavino et al. (2021) for the case of static disk chemical models.

C. PARAMETER DEPENDENCE

C.1. Cosmic-ray ionization rate

In the models presented in Section 3, the galactic cosmic-ray ionization rate was assumed to be $\xi_{\text{CR}} = 10^{-18} \text{ s}^{-1}$. Here we explore the impact of assumed val-

ues of ξ_{CR} on our results. For this sake, we reran the static model and the full model with $\xi_{\text{CR}} = 10^{-16} \text{ s}^{-1}$. There has been no clear observational evidence of higher value of ξ_{CR} in disks than that in the dense ISM ($\sim 10^{-17} \text{ s}^{-1}$). Cleaves et al. (2015) concluded that the emission lines of HCO^+ and N_2H^+ from the TW Hya disk are best reproduced by the model with low CR ionization rate of 10^{-19} s^{-1} . Seifert et al. (2021) concluded that ξ_{CR} in the inner 100 au regions of the IM Lup disk is 10^{-20} s^{-1} by modeling HCO^+ and N_2H^+ emission, while that in the outer regions is $\gtrsim 10^{-17} \text{ s}^{-1}$. Aikawa et al. (2021) concluded that $\xi_{\text{CR}} \gtrsim 10^{-18} \text{ s}^{-1}$ in the disks around IM Lup, AS 209, and HD 163296 on the basis of the comparisons between observationally derived column densities of HCO^+ , N_2H^+ , and N_2D^+ and those predicted by a generic disk model (Aikawa et al. 2018). Then the assumed value of 10^{-16} s^{-1} may be considered as an upper limit of ξ_{CR} in the Class II disk environments.

Figure A4 compares the depletion factors of carbon and nitrogen in the models with $\xi_{\text{CR}} = 10^{-16} \text{ s}^{-1}$ with those in the models with $\xi_{\text{CR}} = 10^{-18} \text{ s}^{-1}$ at 1 Myr. In the static model case, the model with $\xi_{\text{CR}} = 10^{-16} \text{ s}^{-1}$ shows higher depletion factors of carbon and nitrogen in particular inside the CO snowline ($\lesssim 30$ au) and N_2 snowline ($\lesssim 50$ au), respectively, although the depletion factors are less than ~ 10 . This is because the cosmic-ray driven chemistry converts gas-phase CO and gas-phase N_2 near the midplane, where stellar UV and X-ray cannot penetrate, into less volatile icy molecules. The timescale of the chemistry (τ_{CRchem}) is longer than 1 Myr when $\xi_{\text{CR}} = 10^{-18} \text{ s}^{-1}$, whereas the timescale is the order of 10^5 yr when $\xi_{\text{CR}} = 10^{-16} \text{ s}^{-1}$ (see Section 4.1). In the full model case, the assumed value of ξ_{CR} does not significantly affect the depletion factors of carbon and nitrogen, because τ_{CRchem} is larger than τ_{phd} and τ_{mix} even when $\xi_{\text{CR}} = 10^{-16} \text{ s}^{-1}$. Therefore, we conclude that the cosmic-ray ionization rate is less important for

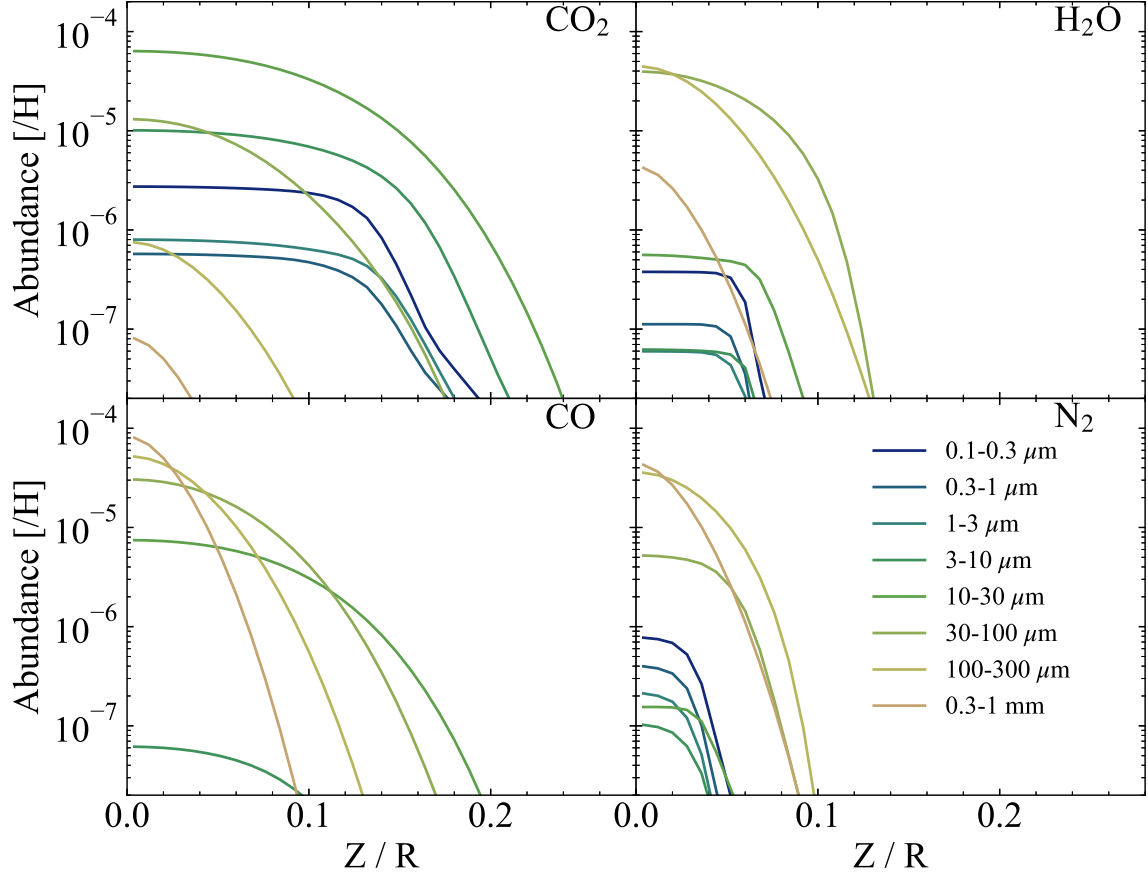


Figure A2. Abundances of CO_2 , CO , H_2O , and N_2 ices on 8 dust populations at $R = 80$ au at 1 Myr in the full model.

the chemistry of carbon (and nitrogen) depletion in the warm gas ($\gtrsim 20$ K) than had been previously thought, when the dust grains have settled and UV radiation penetrate close to the midplane. However, the cosmic-rays are the important parameter for determining the turbulence state of protoplanetary disks, since they control the ionization rate and the status of the magnetorotational instability (e.g., Sano et al. 2000). Thus the cosmic-rays still indirectly play a key role in the carbon and nitrogen depletion through turbulence.

C.2. Maximum and minimum sizes of dust grains

In the models presented in Section 3, the maximum size of dust grains (a_{max}) is fixed to be 1 mm, as often assumed in disk chemical models (e.g., Zhang et al. 2021). On the other hand, (sub)millimeter polarization observations of some disks have suggested that a_{max} is $\sim 100 \mu\text{m}$ (e.g., Kataoka et al. 2016, 2017). Adopting the lower value of a_{max} affects the degrees of carbon and nitrogen depletion by several reasons. First, the dust temperatures are lowered, and thus the efficiency of the vertical cold finger effect is increased. Second, on the other hand, the relative fraction of the cross section

of small dust grain, which are dynamically couple to the gas, to the total dust cross section increases, lowering the efficiency of the vertical cold finger effect. Third, the mass fraction of large dust grains, which are dynamically decoupled from the gas, decreases, leading to larger amount of excess oxygen to convert CO to CO_2 ice via the chemistry driven by stellar UV (Section 3.1). Finally, the penetration of stellar UV photons is reduced, and the chemical conversion of CO into the CO_2 ice becomes less efficient.

To check the impact of a_{max} on our results, we recalculated the entire modeling processes (Figure 1) with $a_{\text{max}} = 100 \mu\text{m}$ or $10 \mu\text{m}$ as the value of a_{max} affects the disk physical conditions. As shown in the left panel of Figure A5, the overall trends of the carbon and nitrogen depletion, that is the depletion of carbon is more significant than that of nitrogen, are not sensitive to the choice of a_{max} , while the values for $f_{\text{depl}}(\text{C})$ and $f_{\text{depl}}(\text{N})$ are depend on a_{max} . At $R \gtrsim 50$ au, both $f_{\text{depl}}(\text{C})$ and $f_{\text{depl}}(\text{N})$ are lowered with reducing a_{max} . This indicates that the second effect is the most important for the outer regions ($\gtrsim 50$ au), assisted by the forth effect in the case for carbon. At $R \lesssim 50$ au, $f_{\text{depl}}(\text{C})$ is enhanced with re-

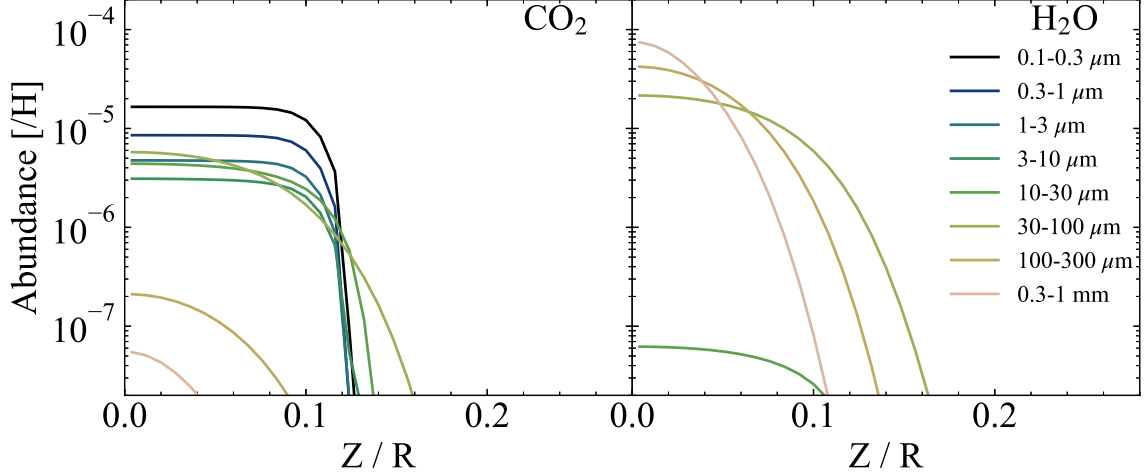


Figure A3. Similar to Figure A3, but for $R = 20$ au. As $R = 20$ au is inside the CO snowline, only CO_2 and H_2O abundances are shown.

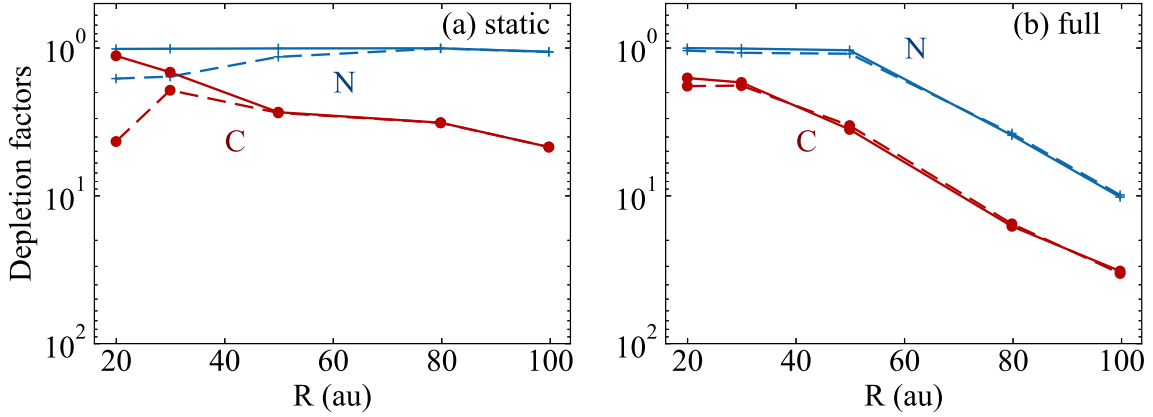


Figure A4. Depletion factors of elemental carbon (red lines) and nitrogen (blue lines) in the model with the enhanced CR ionization rate $\xi_{\text{CR}} = 10^{-16} \text{ s}^{-1}$ (solid lines) and the model with $\xi_{\text{CR}} = 10^{-18} \text{ s}^{-1}$ (dashed lines). Left panel shows the static models, while right panel shows the full models.

ducing a_{max} , while $f_{\text{depl}}(\text{N})$ is insensitive to a_{max} . This result indicates the third effect is the most important at $R \lesssim 50$ au.

The smallest dust grains ($0.1 \mu\text{m}$) in our models are not fully dynamically coupled with gas (see panel c in

Figure 2). To check the impact of the presence of even smaller dust grains, we also recalculated the entire modeling processes with $a_{\text{min}} = 0.01 \mu\text{m}$ rather than $a_{\text{min}} = 0.1 \mu\text{m}$. We confirmed that adopting the smaller value of a_{min} does not affect the depletion factors significantly (right panel of Figure A5).

REFERENCES

- Aikawa, Y., Furuya, K., Hincelin, U., & Herbst, E. 2018, ApJ, 855, 119, doi: [10.3847/1538-4357/aaad6c](https://doi.org/10.3847/1538-4357/aaad6c)
- Aikawa, Y., Furuya, K., Nomura, H., & Qi, C. 2015, ApJ, 807, 120, doi: [10.1088/0004-637X/807/2/120](https://doi.org/10.1088/0004-637X/807/2/120)
- Aikawa, Y., Cataldi, G., Yamato, Y., et al. 2021, ApJS, 257, 13, doi: [10.3847/1538-4365/ac143c](https://doi.org/10.3847/1538-4365/ac143c)
- Akimkin, V., Zhukovska, S., Wiebe, D., et al. 2013, ApJ, 766, 8, doi: [10.1088/0004-637X/766/1/8](https://doi.org/10.1088/0004-637X/766/1/8)
- Anderson, D. E., Blake, G. A., Bergin, E. A., et al. 2019, ApJ, 881, 127, doi: [10.3847/1538-4357/ab2cb5](https://doi.org/10.3847/1538-4357/ab2cb5)
- Andrews, S. M., Wilner, D. J., Hughes, A. M., et al. 2012, ApJ, 744, 162, doi: [10.1088/0004-637X/744/2/162](https://doi.org/10.1088/0004-637X/744/2/162)
- Ansdell, M., Williams, J. P., van der Marel, N., et al. 2016, ApJ, 828, 46, doi: [10.3847/0004-637X/828/1/46](https://doi.org/10.3847/0004-637X/828/1/46)
- Bai, X.-N., & Goodman, J. 2009, ApJ, 701, 737, doi: [10.1088/0004-637X/701/1/737](https://doi.org/10.1088/0004-637X/701/1/737)

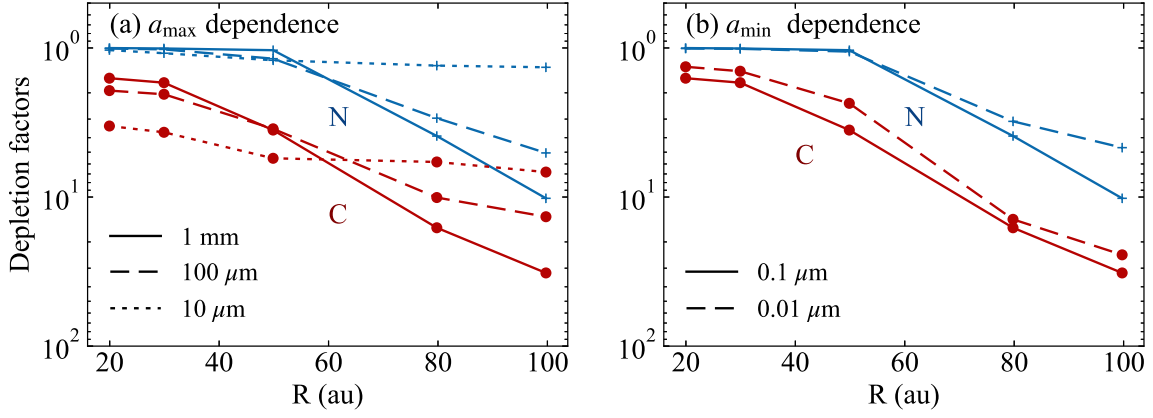


Figure A5. Dependence of depletion factors of elemental carbon (red lines) and nitrogen (blue lines) on a_{\max} (left panel) and a_{\min} (right panel) at 1 Myr. In the left panel, solid, dashed, and dotted lines represent the models with $a_{\max} = 1$ mm, 100 μm , and 10 μm , respectively. In the right panel, solid and dashed lines represent the models with $a_{\min} = 0.1$ μm and 0.01 μm , respectively.

Bergin, E. A., Cleeves, L. I., Crockett, N., & Blake, G. A. 2014, *Faraday Discussions*, 168, 61, doi: [10.1039/C4FD00003J](https://doi.org/10.1039/C4FD00003J)

Bergin, E. A., Du, F., Cleeves, L. I., et al. 2016, *ApJ*, 831, 101, doi: [10.3847/0004-637X/831/1/101](https://doi.org/10.3847/0004-637X/831/1/101)

Bergin, E. A., Cleeves, L. I., Gorti, U., et al. 2013, *Nature*, 493, 644, doi: [10.1038/nature11805](https://doi.org/10.1038/nature11805)

Bergner, J. B., Öberg, K. I., Bergin, E. A., et al. 2020a, *ApJ*, 896, 176, doi: [10.3847/1538-4357/ab98f7](https://doi.org/10.3847/1538-4357/ab98f7)

—. 2020b, *ApJ*, 898, 97, doi: [10.3847/1538-4357/ab9e71](https://doi.org/10.3847/1538-4357/ab9e71)

Birnstiel, T., Dullemond, C. P., Zhu, Z., et al. 2018, *ApJL*, 869, L45, doi: [10.3847/2041-8213/aaf743](https://doi.org/10.3847/2041-8213/aaf743)

Boogert, A. C. A., Gerakines, P. A., & Whittet, D. C. B. 2015, *ARA&A*, 53, 541, doi: [10.1146/annurev-astro-082214-122348](https://doi.org/10.1146/annurev-astro-082214-122348)

Bosman, A. D., Alarcón, F., Zhang, K., & Bergin, E. A. 2021a, *ApJ*, 910, 3, doi: [10.3847/1538-4357/abe127](https://doi.org/10.3847/1538-4357/abe127)

Bosman, A. D., Walsh, C., & van Dishoeck, E. F. 2018, *A&A*, 618, A182, doi: [10.1051/0004-6361/201833497](https://doi.org/10.1051/0004-6361/201833497)

Bosman, A. D., Alarcón, F., Bergin, E. A., et al. 2021b, *ApJS*, 257, 7, doi: [10.3847/1538-4365/ac1435](https://doi.org/10.3847/1538-4365/ac1435)

Brauer, F., Dullemond, C. P., & Henning, T. 2008, *A&A*, 480, 859, doi: [10.1051/0004-6361:20077759](https://doi.org/10.1051/0004-6361:20077759)

Cleeves, L. I., Bergin, E. A., Qi, C., Adams, F. C., & Öberg, K. I. 2015, *ApJ*, 799, 204, doi: [10.1088/0004-637X/799/2/204](https://doi.org/10.1088/0004-637X/799/2/204)

Cleeves, L. I., Öberg, K. I., Wilner, D. J., et al. 2018, *ApJ*, 865, 155, doi: [10.3847/1538-4357/aade96](https://doi.org/10.3847/1538-4357/aade96)

Dionatos, O., Woitke, P., Güdel, M., et al. 2019, *A&A*, 625, A66, doi: [10.1051/0004-6361/201832860](https://doi.org/10.1051/0004-6361/201832860)

Draine, B. T. 1978, *ApJS*, 36, 595, doi: [10.1086/190513](https://doi.org/10.1086/190513)

Draine, B. T., & Li, A. 2007, *ApJ*, 657, 810, doi: [10.1086/511055](https://doi.org/10.1086/511055)

Drozdovskaya, M. N., Walsh, C., van Dishoeck, E. F., et al. 2016, *MNRAS*, 462, 977, doi: [10.1093/mnras/stw1632](https://doi.org/10.1093/mnras/stw1632)

Dullemond, C. P., & Dominik, C. 2004, *A&A*, 421, 1075, doi: [10.1051/0004-6361:20040284](https://doi.org/10.1051/0004-6361:20040284)

Dullemond, C. P., Juhasz, A., Pohl, A., et al. 2012, *RADMC-3D: A multi-purpose radiative transfer tool*, <http://ascl.net/1202.015>

Eistrup, C., Walsh, C., & van Dishoeck, E. F. 2016, *A&A*, 595, A83, doi: [10.1051/0004-6361/201628509](https://doi.org/10.1051/0004-6361/201628509)

Favre, C., Cleeves, L. I., Bergin, E. A., Qi, C., & Blake, G. A. 2013, *ApJL*, 776, L38, doi: [10.1088/2041-8205/776/2/L38](https://doi.org/10.1088/2041-8205/776/2/L38)

Fayolle, E. C., Balfe, J., Loomis, R., et al. 2016, *ApJL*, 816, L28, doi: [10.3847/2041-8205/816/2/L28](https://doi.org/10.3847/2041-8205/816/2/L28)

Flaherty, K., Hughes, A. M., Simon, J. B., et al. 2020, *ApJ*, 895, 109, doi: [10.3847/1538-4357/ab8cc5](https://doi.org/10.3847/1538-4357/ab8cc5)

Flaherty, K. M., Hughes, A. M., Teague, R., et al. 2018, *ApJ*, 856, 117, doi: [10.3847/1538-4357/aab615](https://doi.org/10.3847/1538-4357/aab615)

Flaherty, K. M., Hughes, A. M., Rose, S. C., et al. 2017, *ApJ*, 843, 150, doi: [10.3847/1538-4357/aa79f9](https://doi.org/10.3847/1538-4357/aa79f9)

Furuya, K., & Aikawa, Y. 2014, *ApJ*, 790, 97, doi: [10.1088/0004-637X/790/2/97](https://doi.org/10.1088/0004-637X/790/2/97)

Furuya, K., Aikawa, Y., Nomura, H., Hersant, F., & Wakelam, V. 2013, *ApJ*, 779, 11, doi: [10.1088/0004-637X/779/1/11](https://doi.org/10.1088/0004-637X/779/1/11)

Furuya, K., Drozdovskaya, M. N., Visser, R., et al. 2017, *A&A*, 599, A40, doi: [10.1051/0004-6361/201629269](https://doi.org/10.1051/0004-6361/201629269)

Galametz, M., Maury, A. J., Valdivia, V., et al. 2019, *A&A*, 632, A5, doi: [10.1051/0004-6361/201936342](https://doi.org/10.1051/0004-6361/201936342)

Gavino, S., Dutrey, A., Wakelam, V., et al. 2021, *A&A*, 654, A65, doi: [10.1051/0004-6361/202038788](https://doi.org/10.1051/0004-6361/202038788)

Geers, V. C., Augereau, J.-C., Pontoppidan, K. M., et al. 2006, *A&A*, 459, 545, doi: [10.1051/0004-6361:20064830](https://doi.org/10.1051/0004-6361:20064830)

- Guzmán, V. V., Bergner, J. B., Law, C. J., et al. 2021, *ApJS*, 257, 6, doi: [10.3847/1538-4365/ac1440](https://doi.org/10.3847/1538-4365/ac1440)
- Harsono, D., Bjerke, P., van der Wiel, M. H. D., et al. 2018, *Nature Astronomy*, 2, 646, doi: [10.1038/s41550-018-0497-x](https://doi.org/10.1038/s41550-018-0497-x)
- Harsono, D., Persson, M. V., Ramos, A., et al. 2020, *A&A*, 636, A26, doi: [10.1051/0004-6361/201935994](https://doi.org/10.1051/0004-6361/201935994)
- Heays, A. N., Bosman, A. D., & van Dishoeck, E. F. 2017, *A&A*, 602, A105, doi: [10.1051/0004-6361/201628742](https://doi.org/10.1051/0004-6361/201628742)
- Hunter, J. D. 2007, *Computing in Science & Engineering*, 9, 90, doi: [10.1109/MCSE.2007.55](https://doi.org/10.1109/MCSE.2007.55)
- Igea, J., & Glassgold, A. E. 1999, *ApJ*, 518, 848, doi: [10.1086/307302](https://doi.org/10.1086/307302)
- Ioppolo, S., Palumbo, M. E., Baratta, G. A., & Mennella, V. 2009, *A&A*, 493, 1017, doi: [10.1051/0004-6361/200809769](https://doi.org/10.1051/0004-6361/200809769)
- Jensen, S. S., Jørgensen, J. K., Kristensen, L. E., et al. 2019, *A&A*, 631, A25, doi: [10.1051/0004-6361/201936012](https://doi.org/10.1051/0004-6361/201936012)
- Kama, M., Bruderer, S., van Dishoeck, E. F., et al. 2016, *A&A*, 592, A83, doi: [10.1051/0004-6361/201526991](https://doi.org/10.1051/0004-6361/201526991)
- Kataoka, A., Tsukagoshi, T., Pohl, A., et al. 2017, *ApJL*, 844, L5, doi: [10.3847/2041-8213/aa7e33](https://doi.org/10.3847/2041-8213/aa7e33)
- Kataoka, A., Tsukagoshi, T., Momose, M., et al. 2016, *ApJL*, 831, L12, doi: [10.3847/2041-8205/831/2/L12](https://doi.org/10.3847/2041-8205/831/2/L12)
- Krijt, S., Bosman, A. D., Zhang, K., et al. 2020, *ApJ*, 899, 134, doi: [10.3847/1538-4357/aba75d](https://doi.org/10.3847/1538-4357/aba75d)
- Krijt, S., Schwarz, K. R., Bergin, E. A., & Ciesla, F. J. 2018, *ApJ*, 864, 78, doi: [10.3847/1538-4357/aad69b](https://doi.org/10.3847/1538-4357/aad69b)
- Lee, S., Nomura, H., Furuya, K., & Lee, J.-E. 2021, *ApJ*, 908, 82, doi: [10.3847/1538-4357/abd633](https://doi.org/10.3847/1538-4357/abd633)
- Li, X., Heays, A. N., Visser, R., et al. 2013, *A&A*, 555, A14, doi: [10.1051/0004-6361/201220625](https://doi.org/10.1051/0004-6361/201220625)
- Long, F., Herczeg, G. J., Pascucci, L., et al. 2017, *ApJ*, 844, 99, doi: [10.3847/1538-4357/aa78fc](https://doi.org/10.3847/1538-4357/aa78fc)
- Mawet, D., Absil, O., Montagnier, G., et al. 2012, *A&A*, 544, A131, doi: [10.1051/0004-6361/201219662](https://doi.org/10.1051/0004-6361/201219662)
- McClure, M. K., Bergin, E. A., Cleeves, L. I., et al. 2016, *ApJ*, 831, 167, doi: [10.3847/0004-637X/831/2/167](https://doi.org/10.3847/0004-637X/831/2/167)
- Meijerink, R., Pontoppidan, K. M., Blake, G. A., Poelman, D. R., & Dullemond, C. P. 2009, *ApJ*, 704, 1471, doi: [10.1088/0004-637X/704/2/1471](https://doi.org/10.1088/0004-637X/704/2/1471)
- Miotello, A., Testi, L., Lodato, G., et al. 2014, *A&A*, 567, A32, doi: [10.1051/0004-6361/201322945](https://doi.org/10.1051/0004-6361/201322945)
- Miotello, A., van Dishoeck, E. F., Williams, J. P., et al. 2017, *A&A*, 599, A113, doi: [10.1051/0004-6361/201629556](https://doi.org/10.1051/0004-6361/201629556)
- Miotello, A., Facchini, S., van Dishoeck, E. F., et al. 2019, *A&A*, 631, A69, doi: [10.1051/0004-6361/201935441](https://doi.org/10.1051/0004-6361/201935441)
- Musiolik, G., Teiser, J., Jankowski, T., & Wurm, G. 2016a, *ApJ*, 818, 16, doi: [10.3847/0004-637X/818/1/16](https://doi.org/10.3847/0004-637X/818/1/16)
- . 2016b, *ApJ*, 827, 63, doi: [10.3847/0004-637X/827/1/63](https://doi.org/10.3847/0004-637X/827/1/63)
- Nakagawa, Y., Nakazawa, K., & Hayashi, C. 1981, *Icarus*, 45, 517, doi: [10.1016/0019-1035\(81\)90018-X](https://doi.org/10.1016/0019-1035(81)90018-X)
- Nakatani, R., Liu, H. B., Ohashi, S., et al. 2020, *ApJL*, 895, L2, doi: [10.3847/2041-8213/ab8eaa](https://doi.org/10.3847/2041-8213/ab8eaa)
- Noble, J. A., Dulieu, F., Congiu, E., & Fraser, H. J. 2011, *ApJ*, 735, 121, doi: [10.1088/0004-637X/735/2/121](https://doi.org/10.1088/0004-637X/735/2/121)
- Oba, Y., Watanabe, N., Kouchi, A., Hama, T., & Pirronello, V. 2010, *ApJL*, 712, L174, doi: [10.1088/2041-8205/712/2/L174](https://doi.org/10.1088/2041-8205/712/2/L174)
- Öberg, K. I., & Bergin, E. A. 2021, *PhR*, 893, 1, doi: [10.1016/j.physrep.2020.09.004](https://doi.org/10.1016/j.physrep.2020.09.004)
- Ohashi, S., Kobayashi, H., Nakatani, R., et al. 2021, *ApJ*, 907, 80, doi: [10.3847/1538-4357/abd0fa](https://doi.org/10.3847/1538-4357/abd0fa)
- Persson, M. V., Jørgensen, J. K., & van Dishoeck, E. F. 2012, *A&A*, 541, A39, doi: [10.1051/0004-6361/201117917](https://doi.org/10.1051/0004-6361/201117917)
- Ruaud, M., & Gorti, U. 2019, *ApJ*, 885, 146, doi: [10.3847/1538-4357/ab4996](https://doi.org/10.3847/1538-4357/ab4996)
- Ruaud, M., Gorti, U., & Hollenbach, D. J. 2022, *ApJ*, 925, 49, doi: [10.3847/1538-4357/ac3826](https://doi.org/10.3847/1538-4357/ac3826)
- Sano, T., Miyama, S. M., Umebayashi, T., & Nakano, T. 2000, *ApJ*, 543, 486, doi: [10.1086/317075](https://doi.org/10.1086/317075)
- Seifert, R. A., Cleeves, L. I., Adams, F. C., & Li, Z.-Y. 2021, *ApJ*, 912, 136, doi: [10.3847/1538-4357/abf09a](https://doi.org/10.3847/1538-4357/abf09a)
- Semenov, D., & Wiebe, D. 2011, *ApJS*, 196, 25, doi: [10.1088/0067-0049/196/2/25](https://doi.org/10.1088/0067-0049/196/2/25)
- Shakura, N. I., & Sunyaev, R. A. 1973, *A&A*, 500, 33
- Sheehan, P. D., & Eisner, J. A. 2018, *ApJ*, 857, 18, doi: [10.3847/1538-4357/aaae65](https://doi.org/10.3847/1538-4357/aaae65)
- Stevenson, D. J., & Lunine, J. I. 1988, *Icarus*, 75, 146, doi: [https://doi.org/10.1016/0019-1035\(88\)90133-9](https://doi.org/10.1016/0019-1035(88)90133-9)
- Takeuchi, T., & Lin, D. N. C. 2002, *ApJ*, 581, 1344, doi: [10.1086/344437](https://doi.org/10.1086/344437)
- Teague, R., Guilloteau, S., Semenov, D., et al. 2016, *A&A*, 592, A49, doi: [10.1051/0004-6361/201628550](https://doi.org/10.1051/0004-6361/201628550)
- Trapman, L., Zhang, K., van 't Hoff, M. R. L., Hogerheijde, M. R., & Bergin, E. A. 2022, arXiv e-prints, arXiv:2201.09900. <https://arxiv.org/abs/2201.09900>
- Umebayashi, T., & Nakano, T. 1981, *PASJ*, 33, 617
- Van Clepper, E., Bergner, J. B., Bosman, A. D., Bergin, E., & Ciesla, F. J. 2022, *ApJ*, 927, 206, doi: [10.3847/1538-4357/ac511b](https://doi.org/10.3847/1538-4357/ac511b)
- van 't Hoff, M. L. R., van Dishoeck, E. F., Jørgensen, J. K., & Calcutt, H. 2020, *A&A*, 633, A7, doi: [10.1051/0004-6361/201936839](https://doi.org/10.1051/0004-6361/201936839)
- Vasyunin, A. I., Wiebe, D. S., Birnstiel, T., et al. 2011, *ApJ*, 727, 76, doi: [10.1088/0004-637X/727/2/76](https://doi.org/10.1088/0004-637X/727/2/76)
- Visser, R., van Dishoeck, E. F., & Black, J. H. 2009, *A&A*, 503, 323, doi: [10.1051/0004-6361/200912129](https://doi.org/10.1051/0004-6361/200912129)

- Watanabe, N., & Kouchi, A. 2002, *ApJ*, 567, 651, doi: [10.1086/338491](https://doi.org/10.1086/338491)
- Weingartner, J. C., & Draine, B. T. 2001, *ApJ*, 548, 296, doi: [10.1086/318651](https://doi.org/10.1086/318651)
- Willacy, K. 2007, *ApJ*, 660, 441, doi: [10.1086/512796](https://doi.org/10.1086/512796)
- Wolf, S. 2003, *ApJ*, 582, 859, doi: [10.1086/344710](https://doi.org/10.1086/344710)
- Xu, R., Bai, X.-N., & Öberg, K. 2017, *ApJ*, 835, 162, doi: [10.3847/1538-4357/835/2/162](https://doi.org/10.3847/1538-4357/835/2/162)
- Youdin, A. N., & Lithwick, Y. 2007, *Icarus*, 192, 588, doi: [10.1016/j.icarus.2007.07.012](https://doi.org/10.1016/j.icarus.2007.07.012)
- Zhang, K., Bergin, E. A., Schwarz, K., Krijt, S., & Ciesla, F. 2019, *ApJ*, 883, 98, doi: [10.3847/1538-4357/ab38b9](https://doi.org/10.3847/1538-4357/ab38b9)
- Zhang, K., Booth, A. S., Law, C. J., et al. 2021, *ApJS*, 257, 5, doi: [10.3847/1538-4365/ac1580](https://doi.org/10.3847/1538-4365/ac1580)
- Zhang, K., Schwarz, K. R., & Bergin, E. A. 2020, *ApJL*, 891, L17, doi: [10.3847/2041-8213/ab7823](https://doi.org/10.3847/2041-8213/ab7823)